https://doi.org/10.5194/egusphere-2026-3730
Preprint. Discussion started: 17 July 2026

Evaluating CH_4 retrieval methods for hyperspectral images from EnMAP

Leonie Olivia Scheidweiler[1], Ida Jandl[2, 3], Lukas Häffner[1, 4], Marvin Knapp[5, 6], Lennart Resch[1], Benedikt Löw[1], Christian Mielke[4], Sanam N. Vardag[1, 7], and André Butz[1, 7, 8]

[1]Institute of Environmental Physics, Heidelberg University, Heidelberg, Germany
[2]School of Geography, Earth and Atmospheric Sciences, University of Melbourne, Melbourne, Australia
[3]CSIRO Environment, Aspendale, Melbourne, Australia
[4]German Environment Agency, Dessau-Roßlau, Germany
[5]Environmental Defense Fund, New York, USA
[6]School of Engineering and Applied Science, Harvard University, Cambridge, USA
[7]Heidelberg Center for the Environment (HCE), Heidelberg University, Heidelberg, Germany
[8]Interdisciplinary Center for Scientific Computing, Heidelberg University, Heidelberg, Germany

Correspondence: Leonie Olivia Scheidweiler (leonie.scheidweiler@iup.uni-heidelberg.de)

Abstract. The Environmental Mapping and Analysis Program (EnMAP) satellite carries a hyperspectral instrument that is able to measure methane (CH_4) plumes of localized hotspot sources from which facility-scale emission rates can be estimated. Here, we implement and evaluate three retrieval techniques for scenes with different complexity and source strengths and discuss the differences and implications for emission estimation. These techniques are (i) RemoTeC, a physics-based retrieval that relies on pixel-wise radiative transfer calculations; (ii) a matched-filter retrieval that exploits the spectral covariance of a scene to detect CH_4 enhancements; and (iii) a hybrid retrieval that incorporates spectral covariance information into RemoTeC, thereby combining the strengths of approaches i) and ii).

RemoTeC and the hybrid method yield similar emission estimates, with the hybrid method exhibiting lower statistical noise. The enhancements retrieved by the matched filter have the lowest statistical noise. For sources with emission rates larger than $\sim 3\,\mathrm{t\,h^{-1}}$, the matched filter yields source strength estimates similar to the physics-based retrievals. For weaker sources, the matched filter estimates larger emission rates than the physics-based retrievals, with deviations being on the order of the emission rate itself. While the matched filter effectively suppresses regular and recurring spectral albedo structures, its performance degrades in the presence of statistically rare spectral features. In contrast, the hybrid retrieval more reliably accounts for such albedo-induced artifacts.

Our results demonstrate that retrieval methodology can significantly influence methane emission estimates, particularly in challenging scenes. The matched filter is well suited for rapid quantification of strong emission sources, whereas the physics-based approaches provide greater robustness under difficult observational conditions and for weak emitters. The hybrid retrieval offers the best overall performance by combining the mechanistic rigor of radiative transfer modeling with the noise-reduction benefits of covariance-based methods.

https://doi.org/10.5194/egusphere-2026-3730
Preprint. Discussion started: 17 July 2026

1 Introduction

In the face of anthropogenic global warming, the Paris Agreement (2016) sets a legally binding goal for stabilizing the greenhouse gas concentrations in the atmosphere. Its aim is to limit the temperature increase when compared to pre-industrial levels to well below 2 °C. The total anthropogenic effective radiative forcing in 2019 was $2.72\,\mathrm{W\,m^{-2}}$. The contribution of methane (CH_4) was $0.54\,\mathrm{W\,m^{-2}}$, making it the second largest contributor after carbon dioxide (CO_2) (IPCC, 2021; Saunois et al., 2025).

While the emissions of both greenhouse gases need to be reduced, CH_4 is an ideal candidate for slowing down global warming on a short time scale (Nisbet et al., 2020; IPCC, 2022) due to its lifetime in the atmosphere of roughly 12 years and its global warming potential (GWP-20) of roughly 80 times that of CO_2 on a 20 year time scale (IPCC, 2021). To this end, more than 150 countries signed the Global Methane Pledge (2021), which is an international agreement with the goal of reducing global CH_4 emissions by at least 30 % by 2030 when compared to 2020 emissions. Taking quick action and employing currently existing mitigation techniques could prevent half of the expected CH_4 emissions by 2030, with one quarter of the total emissions being prevented at no net cost (Ocko et al., 2021). Independent measurements and validation of greenhouse gas emissions reduction measures play an important role in holding emitters accountable and help close the gap between top-down measurements and bottom-up inventories (Erland et al., 2022).

CH_4 emissions have major contributions from the energy, agriculture, and waste sectors. Emitters in the energy sector mainly include coal, natural gas, and oil, with their emissions originating from extraction, transport, and processing (Saunois et al., 2025; Global Methane Pledge, 2021). Satellite-based absorption spectroscopic measurements provide an important tool for the detection and quantification of emissions by such sources (Jacob et al., 2022). Their area of application depends on the spatial and spectral resolution of the spectroscopic payload, with some being able to investigate individual hotspot facilities.

Satellite missions can be separated into area and point source mappers (Jacob et al., 2022). Area mappers typically have a spatial resolution of several hundred meters up to a few kilometers. They provide global coverage of greenhouse gases every few days, while being able to detect only the strongest of point sources. Area mappers include SCIAMACHY (Bovensmann et al., 1999; Frankenberg et al., 2005), GOSAT/GOSAT-2 (Kuze et al., 2009; Butz et al., 2011; Imasu et al., 2023; Barr et al., 2025), TROPOMI (Veefkind et al., 2012; Hu et al., 2018), and the upcoming CO2M mission (Sierk et al., 2021; Reuter et al., 2025). Satellite missions with a higher spatial resolution are able to resolve the emission plumes of individual facilities at the cost of not being able to provide global and continous coverage. Point mappers include, for example, Hyperion (Folkman et al., 2001; Thompson et al., 2016), GHGSat (Jervis et al., 2021, 2025), PRISMA (Cogliati et al., 2021; Guanter et al., 2021), EnMAP (Guanter et al., 2015; Roger et al., 2024), EMIT (Green and Thompson, 2020; Thorpe et al., 2023), and the upcoming CHIME mission (Nieke et al., 2023).

Many of the currently orbiting point-source mappers initially have been designed for Earth observation with the goal of retrieving parameters like soil moisture, mineral composition, and vegetation traits. Their detectors include spectral channels in the visible and near-infrared wavelength regions, which contain absorption features of atmospheric gases such as CO_2 and CH_4. This allows for retrieving atmospheric concentrations of CO_2 and CH_4 as reported for satellite measurements (e.g.,

https://doi.org/10.5194/egusphere-2026-3730
Preprint. Discussion started: 17 July 2026

Thompson et al., 2016; Cusworth et al., 2019; Irakulis-Loitxate et al., 2021, 2022; Roger et al., 2024) as well as for airborne observations (e.g., Thorpe et al., 2014, 2016; Borchardt et al., 2021, 2025). Measuring the atmospheric concentration enhancements caused by the emission plumes of individual facilities and further using an observed or meteorologically simulated wind field enables the estimation of emission rates as outlined by, for example, Varon et al. (2018).

Retrieval algorithms convert spatially resolved maps of radiometrically calibrated radiance spectra measured by these satellites (typically called the L1B data product) into maps of gas concentration enhancements. Point-source mappers typically have a spectral resolution that does not allow for resolving individual absorption lines of the target gases. Therefore, the challenge is to distinguish between molecular absorption features and wavelength-dependent surface albedo structures, while taking into account other confounding factors such as topographic effects and light path modification due to aerosols. Commonly used algorithms are so-called physics-based algorithms which simulate radiative transfer through the atmosphere for each groundpixel individually (e.g., Frankenberg et al., 2005; Buchwitz et al., 2005; Yoshida et al., 2011; Butz et al., 2011; Parker et al., 2015; Hu et al., 2018; Schneising et al., 2019), and image-processing methods such as matched filters which aim at identifying spectral absorption signatures in the spectral variation across the 2-dimensional scene using only a target signature for the retrieval (e.g., Manolakis et al., 2014; Thompson et al., 2015; Foote et al., 2020; Thorpe et al., 2013).

The advantage of using physics-based retrievals lies in the ability to use a detailed forward model of radiative transfer which includes parameters such as surface albedo, topography, and aerosol scattering. Physics-based retrievals provide information about the absolute gas column. The matched filters, in contrast, are computationally efficient, in addition to making direct use of the statistical variability of the scene by comparing the targeted absorption signatures to the spectral covariance of the scene (Guanter et al., 2015, 2021; Roger et al., 2024; Ayasse et al., 2023). Instead of retrieving the entire gas column, the matched filters only provide information about the gas enhancement relative to an unknown background. For aircraft measurements, Hochstaffl et al. (2023) showed that the strengths of both methods can be combined in a hybrid method that includes the spectral covariance of the scene in the physics-based retrieval.

Here, we present an evaluation of how a physics-based, matched-filter, and a hybrid algorithm perform for a set of CH_4 point-source plumes under typical conditions. To this end, we use EnMAP hyperspectral measurements (Guanter et al., 2015). We use RemoTeC (Butz et al., 2011) as the physics-based algorithm, we implement a matched filter largely following the concepts of Foote et al. (2020), and we further develop RemoTeC into a hybrid method. Section 2 details the retrieval methods. Section 3 describes the methodology for emission estimation. Section 4 defines the set of observations and Section 5 collects our evaluation results. Section 6 concludes the study.

2 Retrieval algorithms

Our retrieval algorithms calculate the CH_4 column enhancement, with the physics-based retrievals also providing information about the total column. We use hyperspectral measurements of reflected sunlight taken under clear-sky conditions using the spectral range between 2110 nm and 2400 nm. For point-source emission estimation, the horizontal extent of the emission plume is resolved by the high spatial resolution of the image, requiring less accuracy than for area mappers of background

https://doi.org/10.5194/egusphere-2026-3730
Preprint. Discussion started: 17 July 2026

CH_4. This allows all algorithms to safely neglect scattering of light by particles in Earth's atmosphere. Molecular absorption dominates over scattering and thermal emission, simplifying radiative transfer for all methods to Beer-Lambert's law

$$L_\lambda = L_{\lambda,0} \cdot \exp(-\tau_\lambda)\,, \tag{1}$$

where L_λ is the spectral radiance after passage of the absorbing medium, $L_{\lambda,0}$ is the incoming spectral radiance, and τ_λ is the absorption optical depth of the gases in the light path. For notational simplicity, the subscript λ indicates that the quantity consists of spectral elements.

2.1 Physics-based retrieval (RemoTeC)

RemoTeC is a radiative transfer and retrieval algorithm developed by Butz et al. (2009) and previously used for retrieving CH_4 concentrations using area mappers such as GOSAT (Butz et al., 2011) and TROPOMI (Hu et al., 2018; Lorente et al., 2021). RemoTeC performs the trace gas retrieval for each spatial pixel in sequence and does not use any statistical information that may be gained by observing the entire scene. For simulating the observed radiances L_λ, the non-scattering variant of RemoTeC uses a forward model F_λ given by

$$F_\lambda = \mathrm{ILS}_{\lambda-\lambda'} * \left(\frac{A_{\lambda'}\cos\theta_\mathrm{s}}{\pi} \cdot L_{\lambda',\mathrm{Sun}} \cdot \exp(-\tau_{\lambda'}) \right), \tag{2}$$

with the spectral albedo polynomial $A_{\lambda'}$, the solar zenith angle θ_s, the top-of-atmosphere solar irradiance spectrum $L_{\lambda',\mathrm{Sun}}$, and the absorption optical depth $\tau_{\lambda'}$ along the the two-way path from the Sun to the ground and up to the satellite. The calculations within the parentheses on the r.h.s. of Equation 2 are carried out line-by-line on a densely sampled wavelength grid λ'. This allows taking non-linearity effects from optically thick absorption lines into account, which is not possible on the spectral grid of the instrument (see Figure 1). $*$ indicates convolution with the instrument line shape $\mathrm{ILS}_{\lambda-\lambda'}$ onto the spectral grid λ of the measurement instrument. The optical depth $\tau_{\lambda'}$ is given by

$$\tau_{\lambda'} = -\sum_\mathrm{g}\sum_l n_{\mathrm{g},l} \cdot \sigma_{\lambda',\mathrm{g},l} \cdot \mathrm{AMF}\,, \tag{3}$$

where $n_{\mathrm{g},l}$ are the partial column densities of the gases g in atmospheric layers l, $\sigma_{\lambda',\mathrm{g},l}$ are their respective absorption cross-sections, and AMF is the geometric air mass factor which is independent of height under the assumed plane-parallel atmospheric layering. It is defined as $\mathrm{AMF} = 1/\cos\theta_\mathrm{s} + 1/\cos\theta_\mathrm{v}$, where θ_v is the viewing zenith angle of the satellite instrument. The auxiliary information for carrying out these calculations is described in further detail in Section 4.2.

RemoTeC minimizes a least-squares cost function with Tikhonov side-constraint according to

$$\hat{\boldsymbol{x}} = \underset{\boldsymbol{x}}{\mathrm{argmin}} \left(\left| \boldsymbol{\Sigma}^{-\frac{1}{2}} (\mathbf{F}(\boldsymbol{x}) - \boldsymbol{L}) \right|^2 + \left| \mathbf{W}(\boldsymbol{x} - \boldsymbol{x}_\mathrm{apr}) \right|^2 \right) \tag{4}$$

to find the optimal set of parameters chained into the state vector $\boldsymbol{x}$. Note that the spectral elements F_λ and L_λ are also merged into the forward model vector $\boldsymbol{F}$ and the measurement vector $\boldsymbol{L}$. The state vector and its prior estimate $\boldsymbol{x}_\mathrm{apr}$ contain the target gas partial columns, the total columns of interfering species, the parameters of the albedo polynomial, and a spectral shift and

https://doi.org/10.5194/egusphere-2026-3730
Preprint. Discussion started: 17 July 2026

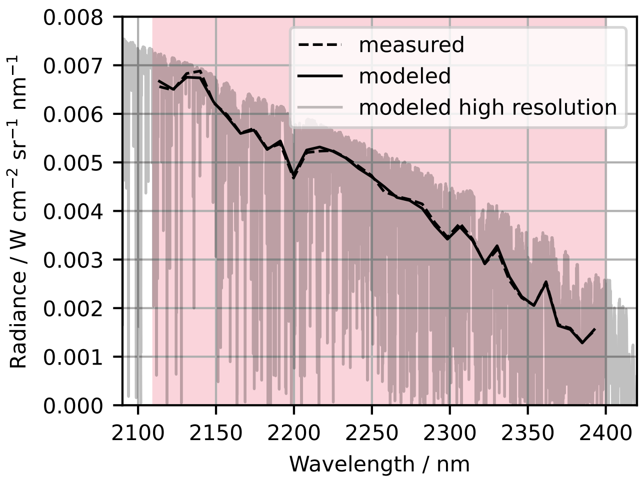

Figure 1. RemoTeC-internal radiance on high-resolution grid as well as convolved onto the spectral grid of the EnMAP instrument, together with measured radiance spectrum. The shaded region is the fit region for this study.

squeeze. $\mathbf{\Sigma}$ is the measurement covariance matrix which, for RemoTeC, is diagonal and calculated according to

$$\Sigma_{\lambda\lambda} = \left(\frac{L_\lambda}{\mathrm{SNR}}\right)^2, \tag{5}$$

with an EnMAP-specific signal-to-noise ratio of $\mathrm{SNR} = 230$ as documented in Storch et al. (2023). The regularization matrix $\mathbf{W}$ is based on the first order difference operator to constrain the vertical gas profiles to mimic the profile shapes of the prior state $\boldsymbol{x}_{\mathrm{apr}}$. Since the forward model is non-linear, the algorithm solves for the optimal state vector iteratively using a Gauss-Newton iteration scheme. Figure 1 shows a simulated and a measured spectrum for an illustrative pixel together with the line-by-line calculations.

Once the retrieval converges, the optimized state informs on the partial column $\mathrm{CH_4}$ densities $n_{\mathrm{CH_4},l}$. Summing over all layers l and dividing by the total column of dry air n_{air} calculated using the ERA5 surface pressure (see Section 4.2) yields the column-average dry-air mole fraction

$$X_{\mathrm{CH_4}} = \frac{\sum_l n_{\mathrm{CH_4},l}}{n_{\mathrm{air}}}. \tag{6}$$

Note that the physics-based methods, including RemoTeC, retrieve the total gas column, which is the sum of the background column and any enhancement. The column enhancement $\Delta X_{\mathrm{CH_4}}$ is determined via line-wise subtraction of the background, taken as the (along-track) median of each detector line.

https://doi.org/10.5194/egusphere-2026-3730
Preprint. Discussion started: 17 July 2026

2.2 Matched filter

For the matched filter, we largely follow the concepts outlined by Foote et al. (2020). The method compares all measured spectra of the 2-dimensional ground scene to a local background, weighs spectral differences by the spectral covariance across the scene, and maps these differences onto the spectral target signature of the trace gas, such as the one illustrated in Figure 2. The target signature is pre-computed and the only external parameter. This approach makes computation simple but does not allow for detailed radiative transfer simulations.

The matched filter requires a background radiance spectrum $L_{\lambda,\mathrm{bg}}$, which is the spectrum that would be measured by the instrument if the target trace gas were at background concentration. Typically, the background spectrum is directly estimated from the scene by averaging over all measured spectra of a given scene, assuming that actual enhancements are statistically rare. Together with the background spectrum, the spectral covariance is calculated as

$$\Sigma_{\lambda\lambda',\mathrm{f}} = \frac{1}{N}\sum_{i=1}^{N}(L_{\lambda,i} - L_{\lambda,\mathrm{bg}})(L_{\lambda',i} - L_{\lambda',\mathrm{bg}}), \tag{7}$$

with i indexing the N spatial pixels used for averaging $L_{\lambda,\mathrm{bg}}$, and f indicating that this covariance matrix typically is filled.

The matched filter assumes that the forward model F_λ that simulates the spectrum L_λ is given by Beer-Lambert's law according to

$$F_\lambda = L_{\lambda,\mathrm{bg}} \cdot \exp(-\Delta X_\mathrm{g} \cdot s_\lambda), \tag{8}$$

where s_λ is the unit absorption spectrum and ΔX_g is the column-averaged dry-air mole fraction enhancement. The unit absorption spectrum describes the logarithmic change in radiance for a given enhancement. Thus, where the physics-based algorithm retrieves the total column, the matched filter forward model only simulates the enhancement. The matched filter operates on quantities at the spectral grid of the instrument λ, which does not allow capturing non-linearities from optically thick lines.

Assuming small absorption signals above background and defining the target signature $t_\lambda = L_{\lambda,\mathrm{bg}} \cdot s_\lambda$, a Taylor expansion yields

$$F_\lambda = L_{\lambda,\mathrm{bg}} \cdot (1 - \Delta X_\mathrm{g} \cdot s_\lambda) = L_{\lambda,\mathrm{bg}} - \Delta X_\mathrm{g} \cdot t_\lambda. \tag{9}$$

A least-squares minimization fits F_λ to the measured spectrum L_λ, solving for the optimal enhancement of the target gas, in our case CH_4, yielding

$$\Delta X_{\mathrm{CH_4}} = \frac{(\boldsymbol{L} - \boldsymbol{L}_\mathrm{bg})^\mathrm{T} \cdot \boldsymbol{\Sigma}_\mathrm{f}^{-1} \cdot \boldsymbol{t}}{\boldsymbol{t}^\mathrm{T} \cdot \boldsymbol{\Sigma}_\mathrm{f}^{-1} \cdot \boldsymbol{t}}, \tag{10}$$

where the spectral elements t_λ, L_λ, $L_{\lambda,\mathrm{bg}}$ and $\Sigma_{\lambda\lambda',\mathrm{f}}$ have been merged into the vectors $\boldsymbol{t}$, $\boldsymbol{L}$, $\boldsymbol{L}_\mathrm{bg}$, and the covariance matrix $\boldsymbol{\Sigma}_\mathrm{f}$, and $^\mathrm{T}$ denotes the transposed vector.

To account for radiometric differences between detector lines, we use a line-wise matched filter, i.e., the averaging for the background spectrum and the calculation of the covariance is carried out along-track for each across-track element individually.

https://doi.org/10.5194/egusphere-2026-3730
Preprint. Discussion started: 17 July 2026

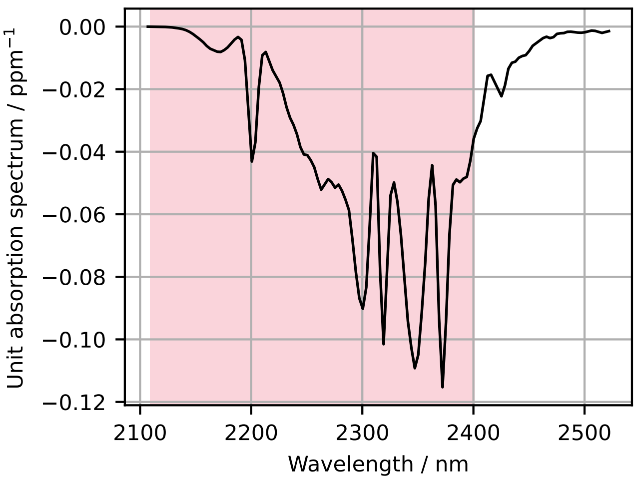

Figure 2. The unit absorption spectrum for CH_4, defined on the spectral grid of the EnMAP instrument. This spectrum shows an example for AMF $= 2$. The shaded region is the fit region for this study.

Further, an albedo correction is performed following Foote et al. (2020), where the target signature is scaled to $\boldsymbol{t}' = \boldsymbol{t} \cdot r$ with

$$r = \frac{\boldsymbol{L} \cdot \boldsymbol{L}_{\mathrm{bg}}}{\boldsymbol{L}_{\mathrm{bg}}^{\mathrm{T}} \cdot \boldsymbol{L}_{\mathrm{bg}}}, \tag{11}$$

for each individual ground pixel, with $\cdot$ denoting the inner product.

In our implementation, we further filter the measurements such that pixels with a brightness below $10\,\%$ of the median brightness in the respective detector line are not considered for the purposes of determining the scene statistics, as very dark pixels may bias the covariance matrix as discussed by Ayasse et al. (2023). Additionally, a simple water mask is generated using the normalized difference water index. A simple cloud filter is implemented using the reflectivity of pixels calculated using the solar irradiance spectrum, in addition to low cloud coverage being considered in the scene selection process. A further filter iteratively excludes enhanced pixels in the calculation of $\boldsymbol{L}_{\mathrm{bg}}$ and $\boldsymbol{\Sigma}_{\mathrm{f}}$ using the noise-equivalent enhancement, removing pixels that are at least three standard deviations above the background (Foote et al., 2020; Pei et al., 2023).

For each spatial pixel, the unit absorption spectrum is read from a lookup table generated using the physics-based forward model of RemoTeC according to Equation 2. Figure 2 shows a typical CH_4 unit absorption spectrum. To calculate it, RemoTeC simulates a background spectrum without enhancement $F_{\lambda,\mathrm{bg}}$ and a spectrum F_λ with an enhancement $\Delta X_{\mathrm{CH_4}}$ and we calculate the unit absorption spectrum s_λ according to

$$s_\lambda = \frac{\ln\left(F_{\lambda,\mathrm{bg}}\right) - \ln\left(F_\lambda\right)}{\Delta X_{\mathrm{CH_4}}}. \tag{12}$$

The unit absorption spectrum is determined via linear interpolation over calculations for CH_4 enhancements up to $20\,\%$ of the background concentration (Foote et al., 2021). These calculations are repeated for various sets of viewing geometries. The

https://doi.org/10.5194/egusphere-2026-3730
Preprint. Discussion started: 17 July 2026

background concentrations are set to $1.930\,\mathrm{ppm}$ for CH_4 and $3\permil$ for water vapor. The pressure and temperature profiles are provided by the ISA Standard Atmosphere 1976 defined by ISO-2533.

2.3 Hybrid retrieval (RemoTeC with scene covariance)

The main advantage of a physics-based retrieval like RemoTeC is that a detailed forward model can be used, including, for example, spectral albedo features, while an advantage of the matched filter is that spatial information about the scene is used in the form of the scene covariance matrix, in addition to lower computational cost. Both retrieval methods model radiative transfer, in this case through Beer-Lambert's law. RemoTeC solves the problem iteratively, being able to account for non-linearity effects from optically thick lines, while the matched filter performs a linear approximation. Both methods can in principle be converted into each other by performing modifications such as introducing an arbitrarily complex lookup table for the unit absorption spectrum.

Here, in addition to the physics-based approach and the matched filter, we set up a hybrid retrieval suggested for aircraft measurements by Hochstaffl et al. (2023) and apply it to EnMAP observations. This retrieval follows the physics-based approach, but, instead of using the diagonal measurement covariance matrix $\mathbf{\Sigma}$, it uses the scene covariance $\mathbf{\Sigma}_\mathrm{f}$ in Equation 4.

For reasons of numerical stability specific to our code, the off-diagonal elements of $\mathbf{\Sigma}_\mathrm{f}$ are multiplied by a factor of 0.95. Using the full scene covariance matrix changes weights of the spectral elements of the measurement in the retrieval. This leads to the retrieval attributing spectral features that the standard retrieval interprets as a trace gas signature as part of the statistical background fluctuations, instead. This should, according to Hochstaffl et al. (2023), result in less noise and better separation of CH_4 from the background when compared to the standard physics-based retrieval.

3 Emission estimation

This section outlines our process for performing emission estimations using the retrieved maps of column enhancements $\Delta X_{\mathrm{CH_4}}$. First, we filter the $\Delta X_{\mathrm{CH_4}}$ maps and identify potential emitters. Then, we run a plume mask algorithm for each detected emission plume. Finally, an emission estimation is performed according to Varon et al. (2018), using external wind speed information.

First, for RemoTeC and the hybrid retrieval, pixels are masked if the retrieval did not converge or if χ^2_red is above a threshold, typically indicating low SNR over water bodies. For all retrievals, pixels are masked if they lie within the water or cloud masks described in Section 2.2. The resulting $\Delta X_{\mathrm{CH_4}}$ maps are first inspected manually to identify plumes. For each plume, the direction of propagation is compared to the $10\,\mathrm{m}$ wind speed taken from ERA5 (see Section 4.2) and the source location is double-checked on Google Maps (2026) to confirm the existence of a possible emitter.

We then generate a plume mask following Kuhlmann et al. (2019), using the matched filter results, as they yield the smoothest enhancement maps among the three retrieval methods. This method compares pixels to a local background, which is characterized by the mean and standard deviation of the enhancements in a manually selected region that does not contain a plume, usually upwind of the source. For a manually selected test region containing the plume, a z-test is performed for each pixel

https://doi.org/10.5194/egusphere-2026-3730
Preprint. Discussion started: 17 July 2026

and its immediate neighborhood to determine if it is part of the background or part of a plume. In the end, the resulting plume mask is smoothed to account for random classification errors (Varon et al., 2018). The local background and plume regions, as well as the critical p-value and the shape of the smoothing kernel are selected individually for each plume, since standardized parameters were hard to find due to the large variability between scenes and source strengths. This approach is sufficient for examining relative differences between the methods. The resulting plume mask is used for the emission estimation for all three retrieval methods.

Varon et al. (2018) describe different methods for calculating emission rates from ΔX_{CH_4} maps. The exact choice for the algorithm is not central to this study, as the same estimation algorithm and the same auxiliary information are used for all retrieval methods, which introduces the same systematic error. This study uses the integrated mass enhancement method. To this end, the local enhancement of each pixel ΔX_{CH_4} is calculated by once again correcting for the local background calculated from the background region, which may differ from zero due to systematic effects across the length of the observed scene. Following Varon et al. (2018), the integrated mass enhancement IME of the target gas inside of the masked plume is calculated according to

$$\mathrm{IME} = \frac{n_{\mathrm{air}} \cdot M_{\mathrm{CH_4}}}{N_{\mathrm{A}}} \cdot \sum_i A_i \cdot \Delta X_{\mathrm{CH_4},i}\,, \tag{13}$$

with the total air mass n_{air} calculated from the ERA5 surface pressure (see Section 4.2), the molar mass of CH_4 $M_{\mathrm{CH_4}} = 16.04\,\mathrm{g\,mol^{-1}}$, and the Avogadro constant N_{A}, multiplied by the sum over all spatial pixels i within the plume mask over the nominal pixel size of the EnMAP satellite corrected by the viewing zenith angle $A_i = (30\,\mathrm{m} \times 30\,\mathrm{m})/\cos(\theta_{\mathrm{v}})$ and the enhancement $\Delta X_{\mathrm{CH_4},i}$. The emission rate Q of the source is then calculated as

$$Q = \frac{v_{\mathrm{eff}}}{L} \cdot \mathrm{IME}\,, \tag{14}$$

where v_{eff} is the effective wind speed in $\mathrm{m\,s^{-1}}$ and L is the effective plume size in m. According to Roger et al. (2024), the effective wind speed for the setup specific to the EnMAP satellite is calculated using

$$v_{\mathrm{eff}} = 0.34 \cdot v_{10} - 0.44\,, \tag{15}$$

where v_{10} is the ERA5 $10\,\mathrm{m}$ wind speed in $\mathrm{m\,s^{-1}}$. Following Varon et al. (2018), we compute the effective plume size L as the square root of the total area of the plume.

The error is calculated using Gaussian error propagation and considers the error of the retrieved enhancement and the error of the wind. For this purpose, the error for the local enhancement of each pixel is set to the standard deviation of the background. The error of the $10\,\mathrm{m}$ wind speed is assumed to be $2\,\mathrm{m\,s^{-1}}$, as suggested by Roger et al. (2024).

4 Data acquisition

Since this study investigates the differences between the retrieval methods, many scenes were selected based on plume detections from previous papers, including most of the scenes investigated by Roger et al. (2024). Further observation targets were

https://doi.org/10.5194/egusphere-2026-3730
Preprint. Discussion started: 17 July 2026

selected based on a prior inventory-driven target evaluation by Häffner (2024) and observations were requested via the EnMAP Instrument Planning Portal (IPP). All scenes used for this study are freely available on the EnMAP EOWEB GeoPortal (EGP).

The physics-based retrievals further require auxiliary data, which is specified below. The matched filter only requires the ILS of the EnMAP instrument and the previously mentioned standard atmosphere in order to pre-compute the unit absorption spectrum lookup table.

4.1 Scene selection

This study observes scenes with CH_4 hotspot sources observed by the EnMAP instrument. The scenes are composed of a small number of tiles arranged in along-track direction, each with a size of 1024×1000 pixels. Each spatial pixel has a nominal sub-satellite size of $30\,\text{m} \times 30\,\text{m}$, resulting in a minimal length and width of the scene of $30\,\text{km}$. Viewing zenith angles for the observed scenes are below $30\,°$. To find systematic differences between the retrieval methods, we investigate a total of 80 plumes across 40 scenes. To closer investigate these differences, we select a small number of these scenes that best showcase the advantages and challenges of the different retrieval methods.

The strongest observed emitters are oil and gas facilities (Roger et al., 2024; Irakulis-Loitxate et al., 2021). Further, this study observes some coal mining regions with underground mining facilities, which are vented through shafts at various locally constrained points (Roger et al., 2024). Another observed scene is the Derweze gas crater (Valverde et al., 2025). The weakest observed sources are landfills, which are distributed over multiple EnMAP pixels, making their emissions difficult to quantify (Roger et al., 2024; Cusworth et al., 2019; Irakulis-Loitxate et al., 2022).

Scenes with detected emission plumes used in this study include 17 scenes covering landfills across India and Spain, 8 Derweze gas crater scenes, 12 scenes covering oil and gas facilities across Turkmenistan, the Permian basin, Algeria, and Iran, and 3 scenes covering coal mines in Poland and China. Furthermore, 3 scenes showing open-pit lignite mines in the Rhenish mining area in Germany are investigated, for which no emission plumes were found but interfering albedo structures are visible in the retrieved images. A full list of used scenes is found in Table A1.

4.2 Auxiliary data

Auxiliary information is required both for the physics-based retrieval of trace gas columns, as well as the creation of the unit absorption spectrum lookup table.

The reference solar spectrum is provided by the TSIS-1 HSRS catalogue (LISIRD, 2022) described by Coddington et al. (2023). We use absorption cross-sections with a Voigt profile, taking into account pressure and temperature broadening. Absorption line parameters for CH_4 and H_2O are provided by the HITRAN 2020 database (HITRAN, 2020) presented by Gordon et al. (2022). The instrument response is a Gaussian function with a spectrally dependent FWHM. The EnMAP L1B data product provides the FWHM for each measured spectral point, which, for the analyzed spectral range, is $\sim 7.8\,\text{nm}$.

Vertical pressure, temperature, and humidity profiles, as well as the wind speeds used in the emission estimation are retrieved from the ERA5 reanalysis product (ECMWF, 2023) per Hersbach et al. (2020). A surface elevation map is downloaded from the ASTER GDEM (METI and NASA, 2019) after ASTER (2019). The a priori profile for CH_4 was taken from the EGG4

https://doi.org/10.5194/egusphere-2026-3730
Preprint. Discussion started: 17 July 2026

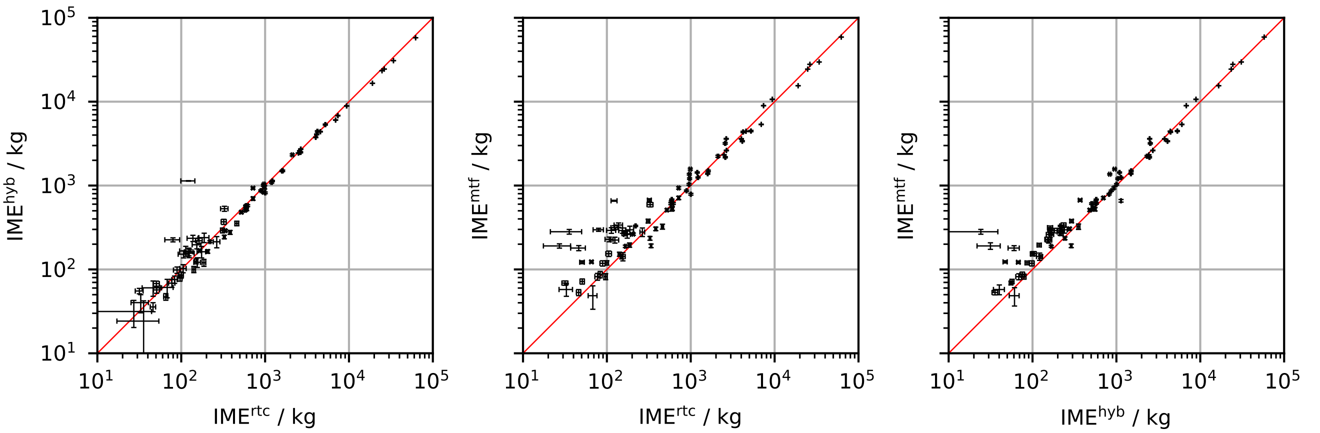

Figure 3. Comparison between IME for all three methods. $\mathrm{IME}^{\mathrm{rtc}}_{\mathrm{CH_4}}$ and $\mathrm{IME}^{\mathrm{hyb}}_{\mathrm{CH_4}}$ show good agreement on the 1:1 line, while $\mathrm{IME}^{\mathrm{mtf}}_{\mathrm{CH_4}}$ estimates larger values below plume masses of $\sim 100\,\mathrm{kg}$.

catalogue (ECMWF, 2021) outlined in Agustí-Panareda et al. (2023). Currently, no EGG4 data exists for the time of the measurements, so EGG4 data from the same day and time in the year 2020 was used. The input data from these sources depends on the spatial location and is interpolated onto the sounding geolocation.

5 Results

Using the outlined methodologies, we examine the scenes listed in Table A1. Where relevant, the results are distinguished by their superscripts between RemoTeC (rtc), matched filter (mtf), and the hybrid retrieval (hyb).

5.1 Comparison of source strength quantification

We determine emission rates for our set of 80 plumes. In the context of comparing the models, IME and Q are equivalent quantities since the same plume mask and wind speed are applied for all three retrievals. Figure 3 shows the IME for all observed plumes correlated between all three retrieval methods. Overall, the three methods agree well with each other in terms of the IME. $\mathrm{IME}^{\mathrm{rtc}}$ and $\mathrm{IME}^{\mathrm{hyb}}$ agree for most of the sources, except for a few outliers. For plumes with an IME smaller than $\sim 100\,\mathrm{kg}$, $\mathrm{IME}^{\mathrm{mtf}}$ tends to be larger than $\mathrm{IME}^{\mathrm{rtc}}$ and $\mathrm{IME}^{\mathrm{hyb}}$.

Transferring these results to the emission rate estimates Q, Figure 4 shows the relative deviation $(\max(Q) - \min(Q))/\overline{Q}$ between the retrieval algorithms for Q of all observed plumes. The retrieval methods yield diverging results for emission rates below $\sim 3\,\mathrm{t\,h^{-1}}$, with differences being roughly on the order of the actual emission estimates, while deviations for stronger sources are generally of the order of a few ten percent. Typically, the matched filter deviates more strongly from RemoTeC and the hybrid method than the latter two from each other. Previous studies defined detection thresholds for point-mappers, such as

https://doi.org/10.5194/egusphere-2026-3730
Preprint. Discussion started: 17 July 2026

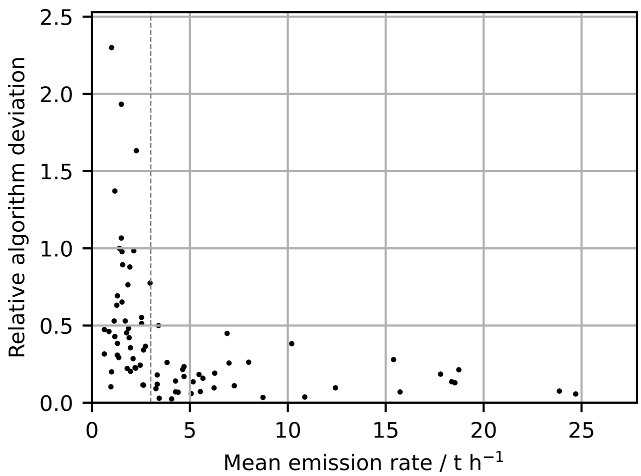

Figure 4. Relative deviation of the emission rate estimates Q between the three retrieval algorithms, ordered by emission rate. Below $\sim 3\,\mathrm{t\,h^{-1}}$, the results of the retrieval algorithms diverge.

EnMAP, on the order of down to $0.5\,\mathrm{t\,h^{-1}}$ (Jacob et al., 2022); our study suggests that methodological differences are relevant for sources up to $3\,\mathrm{t\,h^{-1}}$ and, thus, estimates should be carefully checked for methodological difficulties.

5.2 Systematic features and noise performance

Each data point in Figure 3 and Figure 4 represents an emission estimate for a single source. Figure 5 shows illustrative results for two of these sources: oil and gas facilities in Turkmenistan, which are among the strongest sources observed in this study and have ideal conditions for the quantification of the emission rate. They are located in a desert, where the surface is homogeneous and bright, resulting in a low-noise image. All three retrieval methods perform well under these conditions and the respective emission rate estimates agree within their error estimates. The $\Delta X_{\mathrm{CH_4}}^{\mathrm{rtc}}$ and $\Delta X_{\mathrm{CH_4}}^{\mathrm{hyb}}$ maps show backgrounds which are dominated by statistical noise and do not exhibit any obvious features that correlate with surface albedo patterns. The $\Delta X_{\mathrm{CH_4}}^{\mathrm{mtf}}$ map shows albedo structures both for the different brightness of the sand as well as roads which are located in the observed area. These albedo features are further investigated in Section 5.3, for which the bottom two panels of Figure 5 are relevant.

Figure 6 shows $\Delta X_{\mathrm{CH_4}}$ distributions over the subregion of the scene marked by the rectangle in Figure 5. Here, only background pixels and roads are present and no plumes are located. The hybrid method outperforms RemoTeC in terms of statistical noise, while the mean absolute differences are small. The matched filter shows the smallest statistical background noise. This is due to the covariance matrix weighting spectral features less strongly if they are present in the background statistics. While this smooths background pixels, this has no effect on enhanced pixels, as they are statistically sparse and not represented in the covariance matrix. Where RemoTeC fits both the enhancement and albedo independently for all spatial

https://doi.org/10.5194/egusphere-2026-3730
Preprint. Discussion started: 17 July 2026

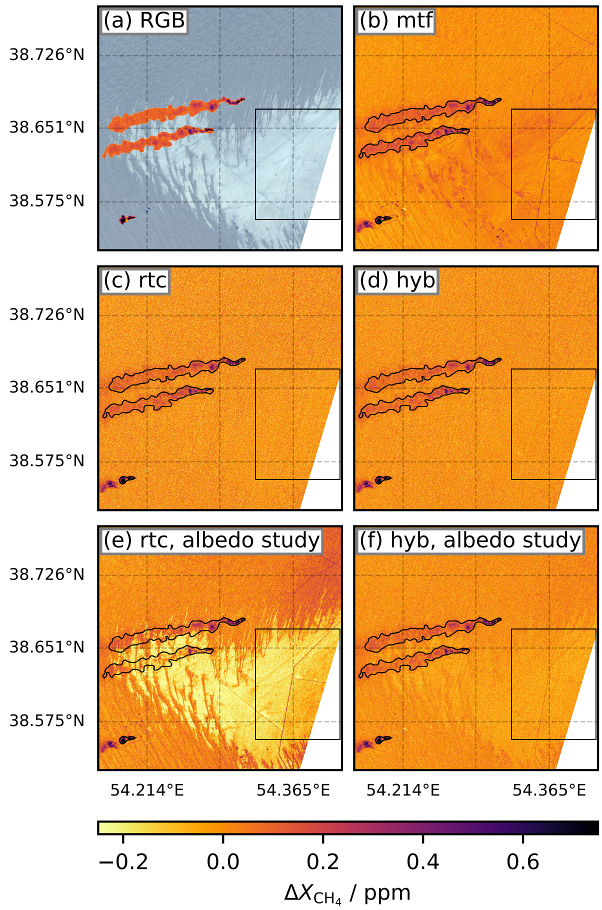

Figure 5. Turkmenistan, 2022-10-02 07:48 UTC, oil and gas facilities. (a) plumes on RGB image; (b) ΔX_{CH_4} Matched Filter (mtf); (c) ΔX_{CH_4} RemoTeC (rtc); (d) ΔX_{CH_4} hybrid method (hyb); (e) ΔX_{CH_4} RemoTeC (rtc) with degraded albedo polynomial; (f) ΔX_{CH_4} hybrid method (hyb) with degraded albedo polynomial. The emissions rate estimates for the northern source are $Q^{\mathrm{mtf}}_{CH_4} = (19.7 \pm 7.1)\,\mathrm{t\,h^{-1}}$, $Q^{\mathrm{rtc}}_{CH_4} = (17.3 \pm 6.3)\,\mathrm{t\,h^{-1}}$, $Q^{\mathrm{hyb}}_{CH_4} = (16.4 \pm 6.0)\,\mathrm{t\,h^{-1}}$. The emission rate estimates for the southern source are $Q^{\mathrm{mtf}}_{CH_4} = (17.9 \pm 6.9)\,\mathrm{t\,h^{-1}}$, $Q^{\mathrm{rtc}}_{CH_4} = (14.7 \pm 5.7)\,\mathrm{t\,h^{-1}}$, $Q^{\mathrm{hyb}}_{CH_4} = (13.6 \pm 5.3)\,\mathrm{t\,h^{-1}}$. The black rectangle denotes the region that is used for the albedo study.

https://doi.org/10.5194/egusphere-2026-3730
Preprint. Discussion started: 17 July 2026

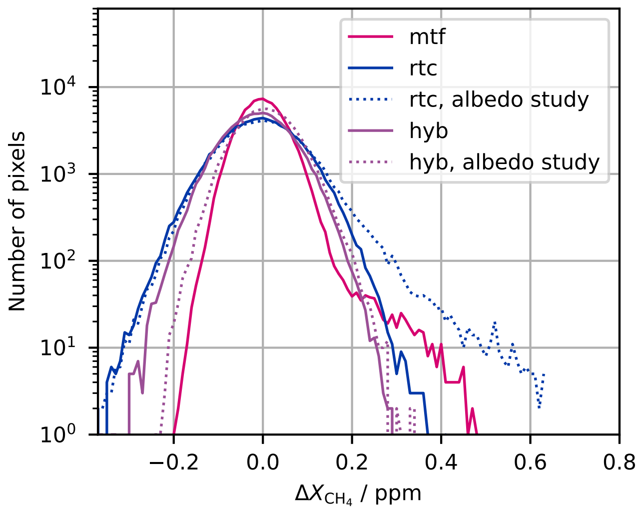

Figure 6. Occurence (logarithmic) of $\Delta X_{\mathrm{CH_4}}$ for the background region of the Turkmenistan scene illustrated by the black rectangle in Figure 5. Solid lines indicate retrievals by the three methods. Dotted lines correspond to sensitivity studies with reduced degree of the albedo polynomial for RemoTeC and the hybrid method.

pixels, the matched filter attributes all enhancements to trace gases, linking all fit parameters via the covariance matrix. The hybrid method retrieves the albedo polynomial independently for each spatial pixel and links the trace gas enhancements, leading to some smoothing. For this specific scene, the albedo features of the roads are only visible in the $\Delta X_{\mathrm{CH_4}}^{\mathrm{mtf}}$ map and show up as a tail in the corresponding distribution.

In contrast to this scene, Figure 7 shows an oil and gas facility in the Permian Basin close to Midland, TX, USA, located in the middle of farmland. Here, the matched filter is able to adjust for the systematic albedo features better than RemoTeC. This shows that the performance of the matched filter with respect to background characterization depends heavily on the observed scene. For the Turkmenistan scene, the roads are a statistically sparse feature and therefore are not sufficiently represented in the scene statistics. The different types of sand are statistically more common and therefore the matched filter is able to better account for them. For the Midland scene, the roads and fields are a spatially regular and repeating feature, resulting in them being included in the scene background both via the mean spectrum as well as the covariance matrix.

In summary, the hybrid method generally outperforms RemoTeC in terms of statistical noise, and the matched filter performs best in terms of statistical noise. The hybrid method outperforms RemoTeC in terms of dealing with systematic features. The performance of the matched filter in regard to systematic features depends on scene homogeneity.

https://doi.org/10.5194/egusphere-2026-3730
Preprint. Discussion started: 17 July 2026

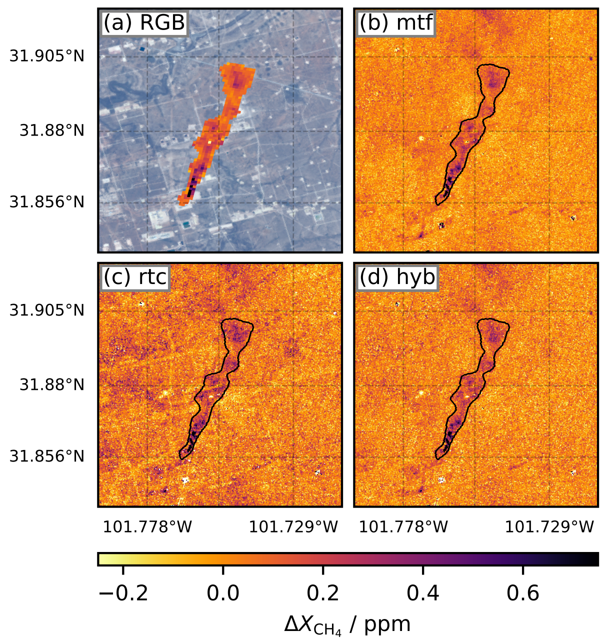

Figure 7. Midland, TX, USA, 2024-02-13 18:12 UTC, oil and gas facility. The emission rate for the source is $Q^{\mathrm{mtf}}_{\mathrm{CH_4}} = (12.5 \pm 3.3)\,\mathrm{t\,h^{-1}}$, $Q^{\mathrm{rtc}}_{\mathrm{CH_4}} = (11.8 \pm 3.1)\,\mathrm{t\,h^{-1}}$, $Q^{\mathrm{hyb}}_{\mathrm{CH_4}} = (13.0 \pm 3.4)\,\mathrm{t\,h^{-1}}$.

5.3 Albedo analysis for asphalt roads

The ability of the physics-based retrievals to fit an albedo polynomial to the measured spectrum allows distinguishing, e.g., roads from the spectral signature of the gas. One possibility to capture such systematic features with a matched filter is the so-called cluster matched filter, in which spatial pixels are grouped according to different surface types, calculating a separate covariance matrix for each group (e.g., Hochstaffl et al., 2023). This oftentimes requires manual selection of the grouping algorithm. This is beneficial for weaker point sources that spatially coincide with systematic structures. Here, we illustrate the effect of surface albedo features by isolating road pixels and comparing their respective radiance spectra to the unit absorption spectrum of $\mathrm{CH_4}$ as well as the reflectivity of asphalt. The black rectangles in Figure 5 define a manually selected subregion of the Turkmenistan scene in which no plume is present and the effect of asphalt roads on the retrieval is visible.

Figure 5 (lower panels) shows the effect of decreasing the spectral albedo polynomial for the RemoTeC and the hybrid retrievals from 4$^{\mathrm{th}}$ degree to 2$^{\mathrm{nd}}$ degree. Lowering the degree of the polynomial reduces the capability of the retrievals to account for the spectral variability of surface reflection and thus, it makes roads and other surface features visible in the $\Delta X_{\mathrm{CH_4}}$ field, with the hybrid method showing less artifacts than RemoTeC. The hybrid retrieval performs significantly better than RemoTeC for the sand-covered surfaces as this is a feature that is statistically frequent across the scene. The matched filter outperforms RemoTeC when using the degraded albedo polynomial since is uses information about the surface features

https://doi.org/10.5194/egusphere-2026-3730
Preprint. Discussion started: 17 July 2026

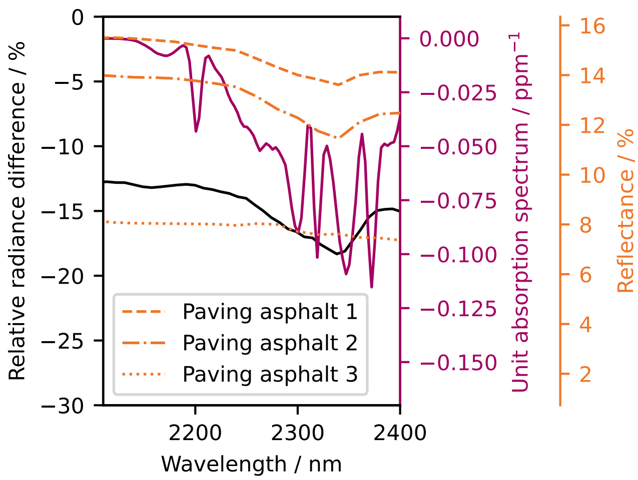

Figure 8. Relative difference of the back-scattered radiance (black, left ordinate) between road and non-road pixels for the albedo study region of the Turkmenistan scene overlaid with the unit absorption spectrum of CH_4 (purple, first right ordinate) and several reflectivity estimates for asphalt surfaces (orange, second right ordinate).

encoded in the mean spectrum and the scene covariance. Comparing the ΔX_{CH_4} distributions for the albedo polynomial of 4th degree (Figure 6, solid lines) to the ΔX_{CH_4} distributions for the albedo polynomial of 2nd degree (Figure 6, dotted lines) after correcting for the median within the subregion reveals that lowering the degree of the albedo polynomial causes RemoTeC to also exhibit a tail corresponding to road pixels. The effect on the hybrid retrieval is less pronounced, being visible mostly in the $\Delta X^{hyb}_{CH_4}$ map.

For qualitative illustration of the influence of road pixels on the retrieval, we examine the radiances for the spatial pixels where roads are located. Road pixels are masked using pixels for which $\Delta X^{mtf}_{CH_4}$ is significantly larger than $\Delta X^{hyb}_{CH_4}$. Figure 8 shows the relative difference in the mean spectrum for all road pixels and all non-road pixels. Furthermore, the figure overlays the unit absorption spectrum of CH_4 and the spectral shape for three different asphalt types downloaded from the ECOSTRESS database (Meerdink et al., 2019; Baldridge et al., 2009). Since the matched filter does not account for the albedo, the similar spectral structure of these quantities explains the erroneously retrieved CH_4 signature above road pixels.

5.4 Performance of retrieval methods for weak plumes

This section investigates the effect of albedo structures on the emission estimation for weak plumes, in particular when the albedo features spatially correlate with the location of the emission plume. Figure 9 shows an illustrative plume emanating from a landfill near the Kanjur Marg suburb of Mumbai, India. The matched filter exhibits a systematic difference when compared to the physics-based retrievals, in particular in the densest part of the plume. For this source, the matched filter

https://doi.org/10.5194/egusphere-2026-3730
Preprint. Discussion started: 17 July 2026

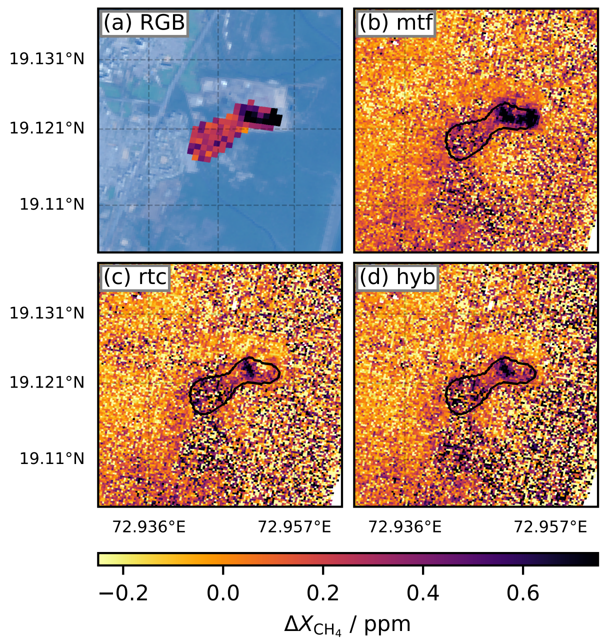

Figure 9. Mumbai, India, 2023-02-14 06:15 UTC, landfill. The emission rate of the source is $Q^{\mathrm{mtf}}_{\mathrm{CH_4}} = (5.2 \pm 4.1)\,\mathrm{t\,h^{-1}}$, $Q^{\mathrm{rtc}}_{\mathrm{CH_4}} = (4.2 \pm 3.3)\,\mathrm{t\,h^{-1}}$, $Q^{\mathrm{hyb}}_{\mathrm{CH_4}} = (4.5 \pm 3.5)\,\mathrm{t\,h^{-1}}$.

retrieves an emission rate $\sim 24\,\%$ larger than the physics-based retrievals, which is large compared to a relative error of $\mathrm{IME^{rtc}}$ and $\mathrm{IME^{hyb}}$ of roughly $2\,\%$ and $3\,\%$, respectively, ignoring any error contributions from the wind speed.

Visually inspecting the source of the emission plume, it is clear that the landfill itself displays spectral surface structures that correlate with the absorption features of CH_4. This feature is statistically sparse across the entire scene and, therefore, it is not captured in the covariance matrix, leading to it being spuriously retrieved as a gas enhancement. The enhancement is not present in RemoTeC and the hybrid method since they account for the spectral reflectivity through their spectral albedo polynomials. The emission plume is one of the weaker plumes investigated in this study, which increases the relative impact of the albedo structures on the emission estimation.

Another notable difference lies in the statistical noise retrieved from the three methods for the different surface types. Located west of the landfill are buildings and roads. These features are regular and repeating throughout the scene, leading to them not causing systematic errors in the $\Delta X_{\mathrm{CH_4}}$ map. They are bright, causing the statistical noise to be relatively small. Located east of the landfill is dark vegetation, which causes significantly larger statistical noise for all three retrieval methods (Guanter et al., 2015; Ayasse et al., 2018). When comparing the matched filter to the physics-based methods, it is clear that the matched filter's inherent smoothing reduces the statistical noise for the low-albedo surface. In this specific scene, RemoTeC shows slightly less statistical noise than the hybrid method. The reason for this is that, for the full scene, half of the pixels at this across-track

https://doi.org/10.5194/egusphere-2026-3730
Preprint. Discussion started: 17 July 2026

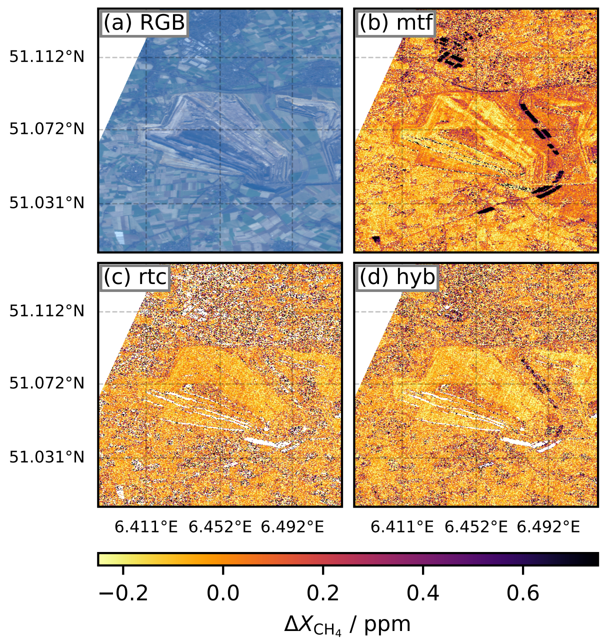

Figure 10. Rhenish mining area, Germany, 2025-12-26 11:18 UTC, Garzweiler open-pit lignite mine.

location contain dark vegetation and half of the pixels consist of buildings, in addition to many pixels being filtered out due to being located above water. Thus, the assumption of a homogeneous background is not valid and the number of valid pixels is insufficient, which introduces errors to the scene statistics (Ayasse et al., 2018).

To conclude, spectral albedo features that are rare throughout the scene show up in $\Delta X^{\mathrm{mtf}}_{\mathrm{CH_4}}$. If these features happen to be located within the plume, they bias the source strength quantification in the matched filter retrieval, while the physics-based retrievals are able to account for them. Additionally, the hybrid method exhibits larger statistical noise when assumptions about homogeneity or a sufficiently large sample size for the background calculation are not valid.

5.5 Investigation of methane emissions and surface features from German open-pit lignite mine

The detection of CH_4 plumes using remote sensing has recently been discussed for coal mining activities (Borchardt et al., 2025; Knapp et al., 2023). This chapter investigates the potential for satellite-borne mapping of CH_4 concentrations over German open-pit lignite mines. Figure 10 shows an exemplary observation of the lignite mine Garzweiler in the Rhenish mining area in Germany.

No emission plumes were detected in any of the investigated open-pit lignite mine scenes. For the other sources investigated by this study, the lowest detected emission rates were $\sim 1\,\mathrm{t\,h^{-1}}$, suggesting that, if point sources are present in this scene, they are below this limit. However, no conclusive emission estimation can be performed, as emissions may originate from a large

https://doi.org/10.5194/egusphere-2026-3730
Preprint. Discussion started: 17 July 2026

area across the open-pit mine. This would invalidate the assumption of a point source, making spatial integration over a larger area necessary. Nonetheless, we analyze several features in this scene.

The statistical noise of the background varies between different regions in the scene. The region within the pit mine is generally bright due to sands, and exhibits some darker features that may be attributed to lignite beds. The northern part of the scene is dominated by vegetation cover, while the southern part is dominated by agricultural fields. Due to the low albedo of the vegetation surrounding the open-pit mine, the statistical noise retrieved by RemoTeC and the hybrid method is larger there than for spatial pixels within the bright pit mine. For RemoTeC, the darkest pixels fail to converge or do not have sufficient fit quality. Within the excavated area, the surface is bright, leading to higher convergence rates and lower noise.

Further, there are different features that cause systematic differences between the retrievals. Located within the scene are logistics facilities with bright roofs north of the pit mine and solar panel arrays surrounding the east side of the pit mine. Certain types of roofs and plastic and paint features were already identified as spectral confusers for CH_4, e.g., by Ayasse et al. (2018). Most notably, $\Delta X^{\mathrm{mtf}}_{\mathrm{CH_4}}$ exhibits significant features correlating with the roofs of the logistics facilities and the solar panels, since they are statistically rare and correlate with the absorption structures of CH_4.

Another observation is that $\Delta X^{\mathrm{hyb}}_{\mathrm{CH_4}}$ also exhibits features for the roofs and solar panels, albeit less significantly than for the matched filter. These features are seemingly not present in $\Delta X^{\mathrm{rtc}}_{\mathrm{CH_4}}$. This, however, is due to RemoTeC failing to converge at all or not having sufficient fit quality for the corresponding spatial pixels. The hybrid method is able to retrieve these spatial pixels due to its inherent smoothing, but introduces a bias during the quantification of these statistically rare features, since their spectral structure is not sufficiently quantified within the scene covariance.

Lastly, the different levels of the pit mine show features visible in the retrieved enhancement maps. The observed effect is strongest for the matched filter, followed by the hybrid method, and weakest for RemoTeC. These may be caused by errors in the light path due to the large variability of the surface elevation in this scene, by albedo features that correlate with the absorption structure of CH_4 together with the lower albedo of the dark lignite beds, or by actual $\Delta X_{\mathrm{CH_4}}$ enhancements. The effect of surface elevation variation is a key difference between the retrieval methods used in this study. The physics-based models consider it via the surface pressure, while the lookup table for the unit absorption spectrum used for the matched filter does not contain surface elevation as a parameter. According to the ASTER elevation model (ASTER, 2019) used in this study, the maximum pit depth is at around $150\,\mathrm{m}$. The elevation data available from this source shows the Garzweiler pit mine as it looked ten years ago (Google Earth, 2026) and is therefore not suited for calculating the true air column. Thus, to exclude any systematic effects on the retrievals due to elevation and focus on analyzing differences between the retrieval methods with respect to albedo features, the results in Figure 10 show $\Delta X^{\mathrm{rtc}}_{\mathrm{CH_4}}$ and $\Delta X^{\mathrm{hyb}}_{\mathrm{CH_4}}$ maps for which the surface elevation has been set to $0\,\mathrm{m}$ and the surface pressure set to $1013.25\,\mathrm{hPa}$, which aligns with the simplifications made for the matched filter. To estimate the systematic error made by this simplification, we use the ideal gas law with standard pressure and standard temperature and calculate the additional air column due to elevation changes. Assuming a maximum depth of $150\,\mathrm{m}$ results in an air column that is $\sim 1.85\,\%$ larger than the surrounding area, causing a theoretical enhancement of $\Delta X_{\mathrm{CH_4}} = 0.035\,\mathrm{ppm}$. This is not significant compared to the background and the systematic features visible in the image. The enhancement structures visible in the $\Delta X^{\mathrm{mtf}}_{\mathrm{CH_4}}$ map are not visible in the $\Delta X^{\mathrm{rtc}}_{\mathrm{CH_4}}$ map and barely visible in the $\Delta X^{\mathrm{hyb}}_{\mathrm{CH_4}}$ map. Therefore, we conclude that,

https://doi.org/10.5194/egusphere-2026-3730
Preprint. Discussion started: 17 July 2026

while part of the retrieved enhancements may be attributed to elevation effects, the features visible in the maps are most likely caused by different surface properties for the individual terraces within the pit mine. However, this example further highlights the difficulty of separating albedo effects from possible true enhancements due to the close spatial correlation between the expected source and surface structures.

We conclude that considering the topography and albedo is particularly beneficial for scenes with complicated topography and many different surface types. Albedo features that spatially correlate with a possible source require careful analysis. For the specific case of the covariance matrix including rare features, the hybrid method may retrieve enhancements for pixels RemoTeC skips, requiring particular care.

6 Conclusions

We compare three retrieval methods for CH_4 enhancements from measurements of the EnMAP satellite, which we use to perform emission estimations for several point sources. This study goes into detail for a number of scenes which showcase different challenges. The methods are the physics-based RemoTeC algorithm, the statistical matched filter retrieval, and a hybrid method that uses the spectral scene covariance of the matched filter with the RemoTeC physics-based algorithm. Examining an ensemble of 80 plumes, we firstly compare the results of the emission estimations for all methods. Further, in order to more directly compare the outputs of the three retrieval methods, we go into detail about the properties of the retrieved enhancement maps.

The two physics-based retrievals result in similar emission estimates throughout the range of emission rates from $\sim 1\,\mathrm{t\,h^{-1}}$ to more than $20\,\mathrm{t\,h^{-1}}$ of CH_4. For sources larger than $\sim 3\,\mathrm{t\,h^{-1}}$, the emission estimates between all three retrieval methods vary within a few ten percent. For weaker sources, the matched filter estimates larger emissions than the physics-based retrievals, with some deviations being on the order of the emission rate itself. Thus, for sources smaller than $3\,\mathrm{t\,h^{-1}}$, differences originating from the selection of the retrieval algorithm need to be considered as a source of error.

We characterize the background in terms of its statistical noise. Both the relative error of the calculated IME and Q as well as the statistical noise of the background are reduced by the introduction of the covariance matrix. The matched filter exhibits the least statistical noise among the retrieval methods, followed by the hybrid method. RemoTeC results in the largest statistical noise.

We also determine the systematic effect of albedo structures on the retrieval, specifying which properties make a scene particularly challenging for the different methods. The performance of the matched filter with respect to systematic background features depends heavily on scene homogeneity. Scenes need to have a sufficient size for the mean spectrum and the scene covariance to capture albedo features, and the matched filter manages to account for spectral surface features only if they are statistically abundant. Since the matched filter attributes all detected radiance changes to the retrieved trace gas, surface features that are statistically rare will be visible as trace gas signals in the resulting $\Delta X_{\mathrm{CH_4}}$ map. This causes problems if they are co-located with actual absorption signals.

https://doi.org/10.5194/egusphere-2026-3730
Preprint. Discussion started: 17 July 2026

Generally, the hybrid method outperforms RemoTeC in terms of separating systematic features that interfere with the spectral structure of the absorbing gas from actual enhancements. For very dark scenes and albedo features that are rare across the scene, it is possible that RemoTeC does not converge with sufficient fit quality, while the hybrid method converges. This may lead to the hybrid method seemingly performing not as well as the basic implementation, which requires caution and manually inspecting the $\Delta X_{\mathrm{CH_4}}$ map.

For the physics-based retrievals, a balance must be found for the degree of the fitted albedo polynomial, which depends, e.g., on the spectral resolution of the used instrument, the observed scenes, and the fit window. An albedo polynomial of insufficient degree will result in the $\Delta X_{\mathrm{CH_4}}$ map showing features for different surface types.

Overall, the matched filter is a suitable tool for performing emission estimations quickly and easily, while the physics-based retrievals may be best for analyzing weak sources under difficult measurement conditions, with the hybrid method outperforming the standard implementation of RemoTeC.

Code and data availability. The code and data are available from the corresponding author upon request.

Appendix A: List of scenes

The complete list of EnMAP scenes used for this study is available in Table A1.

Author contributions. LOS adjusted RemoTeC to work with EnMAP data, implemented a matched filter, and modified RemoTeC to work as a hybrid retrieval, as well as perfomed the emission estimates and studies. IJ previously performed analyses that this work is built upon, and supported with the development and discussion of the three retrieval methods. LH and CM organized the datatake of EnMAP measurements, and gave valuable feedback about the selection of emission sites. MK and LR aided with the development of the matched filter. BL assisted with the development and discussion of RemoTeC adjustments. AB conceptualized the project, AB and SNV supervised the project. Everyone contributed to the authoring and editing of this paper. Special thanks goes to Lisa Cymanek for proof-reading and helpful feedback.

Competing interests. The authors declare that they do not have competing interests.

Acknowledgements. The project is funded by the Federal Ministry of Research, Technology, and Space under grant FKZ 50EE2232. This study acknowledges support from the EU Horizon Europe project AVENGERS (Grant Agreement (GA): 101081322). The authors gratefully acknowledge the data storage service SDS@hd supported by the Ministry of Science, Research and the Arts Baden-Württemberg (MWK) and the German Research Foundation (DFG) through grant INST 35/1503-1 FUGG. The authors acknowledge support by the state of Baden-Württemberg through bwHPC and the German Research Foundation (DFG) through grant INST 35/1597-1 FUGG.

https://doi.org/10.5194/egusphere-2026-3730
Preprint. Discussion started: 17 July 2026

Table A1. Full list of scenes used in the study. Upper list contains scenes in which at least one emission plume was detected. Lower list contains scenes in which no emission plumes were found.

Scene name	Date	Lat/Lon
ahmedabad	2024-06-07	23.013, 72.574
delhi	2022-11-29	28.690, 77.245
delhi	2023-03-09	28.697, 77.173
delhi	2023-04-24	28.620, 77.200
delhi	2024-01-11	28.596, 77.234
delhi	2024-05-18	28.641, 77.150
delhi	2024-05-25	28.635, 77.327
delhi	2024-05-29	28.738, 77.152
delhi	2024-11-27	28.543, 77.124
delhi	2024-12-01	28.672, 77.161
delhi	2025-01-31	28.615, 77.164
delhi	2025-05-11	28.488, 77.134
derweze	2023-06-13	40.311, 58.457
derweze	2024-09-14	40.205, 58.424
derweze	2024-09-22	40.375, 58.472
derweze	2024-11-07	40.246, 58.436
derweze	2024-12-23	40.200, 58.425
derweze	2025-01-31	40.242, 58.438
derweze	2025-02-19	40.260, 58.439
derweze	2025-03-14	40.360, 58.476
hassi messaoud	2022-11-17	31.917, 5.998
hassi messaoud	2024-08-18	31.483, 5.928
hassi messaoud	2024-08-30	31.592, 5.938
hassi messaoud	2025-03-26	31.752, 6.066
hassi messaoud	2025-04-22	31.749, 6.063
khuzestan	2024-11-16	30.296, 47.750
madrid	2024-07-05	40.274, -3.635
madrid	2024-07-13	40.241, -3.647
madrid	2024-12-06	40.258, -3.641
midland	2024-01-20	32.022, -101.796
midland	2024-02-13	32.050, -101.775
mumbai	2023-02-14	19.087, 72.884
mumbai	2024-01-31	19.124, 72.949
pniowek	2025-10-03	49.981, 18.723
shanxi	2022-12-05	36.273, 113.144
shanxi	2023-03-30	36.059, 112.954
turkmenistan	2022-10-02	38.685, 54.244
turkmenistan	2022-10-06	38.643, 54.233
turkmenistan	2024-08-30	38.516, 54.201
turkmenistan	2024-09-11	38.546, 54.215
rhenish mining area	2024-09-19	50.902, 6.229
rhenish mining area	2025-10-02	50.976, 6.246
rhenish mining area	2025-12-26	50.921, 6.547

https://doi.org/10.5194/egusphere-2026-3730
Preprint. Discussion started: 17 July 2026

Contains modified EnMAP data ©DLR 2022-2026. Contains modified Copernicus Climate Change Service information [2022-2026]. Contains modified Copernicus Atmosphere Monitoring Service information [2022-2026]. Neither the European Commission nor the European Centre for Medium-Range Weather Forecasts (ECMWF) is responsible for any use that may be made of the Copernicus information or data it contains. The results presented in this document rely on data from the TSIS-1 Hybrid Solar Reference Spectrum (HSRS) model described in Coddington et al. (2023). The solar spectrum was accessed via the LASP Interactive Solar Irradiance Datacenter LISIRD (2022).

https://doi.org/10.5194/egusphere-2026-3730
Preprint. Discussion started: 17 July 2026

References

Agustí-Panareda, A., Barré, J., Massart, S., Inness, A., Aben, I., Ades, M., Baier, B. C., Balsamo, G., Borsdorff, T., Bousserez, N., Boussetta, S., Buchwitz, M., Cantarello, L., Crevoisier, C., Engelen, R., Eskes, H., Flemming, J., Garrigues, S., Hasekamp, O., Huijnen, V., Jones, L., Kipling, Z., Langerock, B., McNorton, J., Meilhac, N., Noël, S., Parrington, M., Peuch, V.-H., Ramonet, M., Razinger, M., Reuter, M., Ribas, R., Suttie, M., Sweeney, C., Tarniewicz, J., and Wu, L.: Technical note: The CAMS greenhouse gas reanalysis from 2003 to 2020, https://doi.org/10.5194/acp-23-3829-2023, 2023.

ASTER: NASA/METI/AIST/Japan Spacesystems and U.S./Japan ASTER Science Team: ASTER Global Digital Elevation Model V003, distributed by NASA EOSDIS Land Processes Distributed Active Archive Center, https://doi.org/10.5067/ASTER/ASTGTM.003, 2019.

Ayasse, A. K., Thorpe, A. K., Roberts, D. A., Funk, C. C., Dennison, P. E., Frankenberg, C., Steffke, A., and Aubrey, A. D.: Evaluating the effects of surface properties on methane retrievals using a synthetic airborne visible/infrared imaging spectrometer next generation (AVIRIS-NG) image, Remote Sensing of Environment, 215, 386–397, https://doi.org/10.1016/j.rse.2018.06.018, 2018.

Ayasse, A. K., Cusworth, D., O'Neill, K., Fisk, J., Thorpe, A. K., and Duren, R.: Performance and sensitivity of column-wise and pixel-wise methane retrievals for imaging spectrometers, Atmospheric Measurement Techniques, 16, 6065–6074, https://doi.org/10.5194/amt-16-6065-2023, 2023.

Baldridge, A., Hook, S., Grove, C., and Rivera, G.: The ASTER spectral library version 2.0, Remote Sensing of Environment, 113, 711–715, https://doi.org/10.1016/j.rse.2008.11.007, 2009.

Barr, A. G., Landgraf, J., Martinez-Velarte, M., Vrekoussis, M., Sussmann, R., Morino, I., Strong, K., Zhou, M., Velazco, V. A., Ohyama, H., Warneke, T., Hase, F., and Borsdorff, T.: Five years of GOSAT-2 retrievals with RemoTeC: XCO_2 and XCH_4 data products with quality filtering by machine learning, Atmospheric Measurement Techniques, 18, 6093–6123, https://doi.org/10.5194/amt-18-6093-2025, 2025.

Borchardt, J., Gerilowski, K., Krautwurst, S., Bovensmann, H., Thorpe, A. K., Thompson, D. R., Frankenberg, C., Miller, C. E., Duren, R. M., and Burrows, J. P.: Detection and quantification of CH_4 plumes using the WFM-DOAS retrieval on AVIRIS-NG hyperspectral data, Atmospheric Measurement Techniques, 14, 1267–1291, https://doi.org/10.5194/amt-14-1267-2021, 2021.

Borchardt, J., Harris, S. J., Hacker, J. M., Lunt, M., Krautwurst, S., Bai, M., Bösch, H., Bovensmann, H., Burrows, J. P., Chakravarty, S., Field, R. A., Gerilowski, K., Huhs, O., Junkermann, W., Kelly, B. F. J., Kumm, M., Lieff, W., McGrath, A., Murphy, A., Schindewolf, J., and Thoböll, J.: Insights into Elevated Methane Emissions from an Australian Open-Cut Coal Mine Using Two Independent Airborne Techniques, Environmental Science & Technology Letters, 12, 397–404, https://doi.org/10.1021/acs.estlett.4c01063, 2025.

Bovensmann, H., Burrows, J. P., Buchwitz, M., Frerick, J., Noël, S., Rozanov, V. V., Chance, K. V., and Goede, A. P. H.: SCIAMACHY: Mission Objectives and Measurement Modes, Journal of the Atmospheric Sciences, 56, 127–150, https://doi.org/10.1175/1520-0469(1999)056<0127:SMOAMM>2.0.CO;2, 1999.

Buchwitz, M., de Beek, R., Burrows, J. P., Bovensmann, H., Warneke, T., Notholt, J., Meirink, J. F., Goede, A. P. H., Bergamaschi, P., Körner, S., Heimann, M., and Schulz, A.: Atmospheric methane and carbon dioxide from SCIAMACHY satellite data: initial comparison with chemistry and transport models, Atmospheric Chemistry and Physics, 5, 941–962, https://doi.org/10.5194/acp-5-941-2005, 2005.

Butz, A., Hasekamp, O. P., Frankenberg, C., and Aben, I.: Retrievals of atmospheric CO2 from simulated space-borne measurements of backscattered near-infrared sunlight: accounting for aerosol effects, Appl. Opt., 48, 3322–3336, https://doi.org/10.1364/AO.48.003322, 2009.

Butz, A., Guerlet, S., Hasekamp, O., Schepers, D., Galli, A., Aben, I., Frankenberg, C., Hartmann, J.-M., Tran, H., Kuze, A., Keppel-Aleks, G., Toon, G., Wunch, D., Wennberg, P., Deutscher, N., Griffith, D., Macatangay, R., Messerschmidt, J., Notholt, J., and Warneke, T.:

https://doi.org/10.5194/egusphere-2026-3730
Preprint. Discussion started: 17 July 2026

Toward accurate CO2 and CH4 observations from GOSAT, Geophysical Research Letters, 38, https://doi.org/10.1029/2011GL047888, 2011.

Coddington, O. M., Richard, E. C., Harber, D., Pilewskie, P., Woods, T. N., Snow, M., Chance, K., Liu, X., and Sun, K.: Version 2 of the TSIS-1 Hybrid Solar Reference Spectrum and Extension to the Full Spectrum, Earth and Space Science, 10, 2022–2637, https://doi.org/10.1029/2022EA002637, 2023.

Cogliati, S., Sarti, F., Chiarantini, L., Cosi, M., Lorusso, R., Lopinto, E., Miglietta, F., Genesio, L., Guanter, L., Damm, A., Pérez-López, S., Scheffler, D., Tagliabue, G., Panigada, C., Rascher, U., Dowling, T., Giardino, C., and Colombo, R.: The PRISMA imaging spectroscopy mission: overview and first performance analysis, Remote Sensing of Environment, 262, 112 499, https://doi.org/10.1016/j.rse.2021.112499, 2021.

Cusworth, D. H., Jacob, D. J., Varon, D. J., Chan Miller, C., Liu, X., Chance, K., Thorpe, A. K., Duren, R. M., Miller, C. E., Thompson, D. R., Frankenberg, C., Guanter, L., and Randles, C. A.: Potential of next-generation imaging spectrometers to detect and quantify methane point sources from space, Atmospheric Measurement Techniques, 12, 5655–5668, https://doi.org/10.5194/amt-12-5655-2019, 2019.

ECMWF: CAMS global greenhouse gas reanalysis (EGG4), https://www.copernicus.eu/en/access-data/copernicus-services-catalogue/cams-global-ghg-reanalysis-egg4, 2021.

ECMWF: Complete ERA5 global atmospheric reanalysis, https://cds.climate.copernicus.eu/cdsapp#!/dataset/reanalysis-era5-complete, 2023.

EnMAP EOWEB GeoPortal (EGP): EnMAP EOWEB GeoPortal (EGP), https://eoweb.dlr.de/egp/, accessed: 2026-04-01.

EnMAP Instrument Planning Portal (IPP): EnMAP Instrument Planning Portal (IPP), https://planning.enmap.org/, accessed: 2026-05-28.

Erland, B. M., Thorpe, A. K., and Gamon, J. A.: Recent Advances Toward Transparent Methane Emissions Monitoring: A Review, Environmental Science & Technology, 56, 16 567–16 581, https://doi.org/10.1021/acs.est.2c02136, 2022.

Folkman, M. A., Pearlman, J., Liao, L. B., and Jarecke, P. J.: EO-1/Hyperion hyperspectral imager design, development, characterization, and calibration, in: Hyperspectral Remote Sensing of the Land and Atmosphere, vol. 4151, pp. 40–51, SPIE, https://doi.org/10.1117/12.417022, 2001.

Foote, M. D., Dennison, P. E., Thorpe, A. K., Thompson, D. R., Jongaramrungruang, S., Frankenberg, C., and Joshi, S. C.: Fast and Accurate Retrieval of Methane Concentration From Imaging Spectrometer Data Using Sparsity Prior, IEEE Transactions on Geoscience and Remote Sensing, 58, 6480–6492, https://doi.org/10.1109/TGRS.2020.2976888, 2020.

Foote, M. D., Dennison, P. E., Sullivan, P. R., O'Neill, K. B., Thorpe, A. K., Thompson, D. R., Cusworth, D. H., Duren, R., and Joshi, S. C.: Impact of Scene-Specific Enhancement Spectra on Matched Filter Greenhouse Gas Retrievals from Imaging Spectroscopy, Remote Sensing of Environment, 264, 112 574, https://doi.org/10.1016/j.rse.2021.112574, arXiv:2107.05578 [physics], 2021.

Frankenberg, C., Meirink, J. F., van Weele, M., Platt, U., and Wagner, T.: Assessing Methane Emissions from Global Space-Borne Observations, Science, 308, 1010–1014, https://doi.org/10.1126/science.1106644, 2005.

Global Methane Pledge: Global Methane Pledge, https://www.globalmethanepledge.org/, 2021.

Google Earth: Google Earth, https://earth.google.com/web/, accessed: 2026-04-01, 2026.

Google Maps: Google Maps, https://maps.google.com/, accessed: 2026-04-01, 2026.

Gordon, I. E., Rothman, L. S., Hargreaves, R. J., Hashemi, R., Karlovets, E. V., Skinner, F. M., Conway, E. K., Hill, C., Kochanov, R. V., Tan, Y., Wcisło, P., Finenko, A. A., Nelson, K., Bernath, P. F., Birk, M., Boudon, V., Campargue, A., Chance, K. V., Coustenis, A., Drouin, B. J., Flaud, J. M., Gamache, R. R., Hodges, J. T., Jacquemart, D., Mlawer, E. J., Nikitin, A. V., Perevalov, V. I., Rotger, M., Tennyson, J., Toon, G. C., Tran, H., Tyuterev, V. G., Adkins, E. M., Baker, A., Barbe, A., Canè, E., Császár, A. G., Dudaryonok, A., Egorov, O., Fleisher,

https://doi.org/10.5194/egusphere-2026-3730
Preprint. Discussion started: 17 July 2026

A. J., Fleurbaey, H., Foltynowicz, A., Furtenbacher, T., Harrison, J. J., Hartmann, J. M., Horneman, V. M., Huang, X., Karman, T., Karns, J., Kassi, S., Kleiner, I., Kofman, V., Kwabia-Tchana, F., Lavrentieva, N. N., Lee, T. J., Long, D. A., Lukashevskaya, A. A., Lyulin, O. M., Makhnev, V. Y., Matt, W., Massie, S. T., Melosso, M., Mikhailenko, S. N., Mondelain, D., Müller, H. S. P., Naumenko, O. V., Perrin, A., Polyansky, O. L., Raddaoui, E., Raston, P. L., Reed, Z. D., Rey, M., Richard, C., Tóbiás, R., Sadiek, I., Schwenke, D. W., Starikova, E., Sung, K., Tamassia, F., Tashkun, S. A., Vander Auwera, J., Vasilenko, I. A., Vigasin, A. A., Villanueva, G. L., Vispoel, B., Wagner, G., Yachmenev, A., and Yurchenko, S. N.: The HITRAN2020 molecular spectroscopic database, Journal of Quantitative Spectroscopy and Radiative Transfer, 277, 107949, https://doi.org/10.1016/j.jqsrt.2021.107949, 2022.

Green, R. O. and Thompson, D. R.: An Earth Science Imaging Spectroscopy Mission: The Earth Surface Mineral Dust Source Investigation (EMIT), in: IGARSS 2020 - 2020 IEEE International Geoscience and Remote Sensing Symposium, pp. 6262–6265, ISSN 2153-7003, https://doi.org/10.1109/IGARSS39084.2020.9323741, iSSN: 2153-7003, 2020.

Guanter, L., Kaufmann, H., Segl, K., Foerster, S., Rogass, C., Chabrillat, S., Kuester, T., Hollstein, A., Rossner, G., Chlebek, C., Straif, C., Fischer, S., Schrader, S., Storch, T., Heiden, U., Mueller, A., Bachmann, M., Mühle, H., Müller, R., Habermeyer, M., Ohndorf, A., Hill, J., Buddenbaum, H., Hostert, P., Linden, S. V. d., Leitão, P. J., Rabe, A., Doerffer, R., Krasemann, H., Xi, H., Mauser, W., Hank, T., Locherer, M., Rast, M., Staenz, K., and Sang, B.: The EnMAP Spaceborne Imaging Spectroscopy Mission for Earth Observation, Remote Sensing, 7, 8830–8857, https://doi.org/10.3390/rs70708830, 2015.

Guanter, L., Irakulis-Loitxate, I., Gorroño, J., Sánchez-García, E., Cusworth, D. H., Varon, D. J., Cogliati, S., and Colombo, R.: Mapping methane point emissions with the PRISMA spaceborne imaging spectrometer, Remote Sensing of Environment, 265, 112 671, https://doi.org/10.1016/j.rse.2021.112671, 2021.

Hersbach, H., Bell, B., Berrisford, P., Hirahara, S., Horányi, A., Muñoz-Sabater, J., Nicolas, J., Peubey, C., Radu, R., Schepers, D., Simmons, A., Soci, C., Abdalla, S., Abellan, X., Balsamo, G., Bechtold, P., Biavati, G., Bidlot, J., Bonavita, M., De Chiara, G., Dahlgren, P., Dee, D., Diamantakis, M., Dragani, R., Flemming, J., Forbes, R., Fuentes, M., Geer, A., Haimberger, L., Healy, S., Hogan, R. J., Hólm, E., Janisková, M., Keeley, S., Laloyaux, P., Lopez, P., Lupu, C., Radnoti, G., de Rosnay, P., Rozum, I., Vamborg, F., Villaume, S., and Thépaut, J.-N.: The ERA5 global reanalysis, Quarterly Journal of the Royal Meteorological Society, 146, 1999–2049, https://doi.org/10.1002/qj.3803, 2020.

HITRAN: HITRANonline, https://hitran.org/lbl/, 2020.

Hochstaffl, P., Schreier, F., Köhler, C. H., Baumgartner, A., and Cerra, D.: Methane retrievals from airborne HySpex observations in the shortwave infrared, Atmospheric Measurement Techniques, 16, 4195–4214, https://doi.org/10.5194/amt-16-4195-2023, 2023.

Hu, H., Landgraf, J., Detmers, R., Borsdorff, T., Aan de Brugh, J., Aben, I., Butz, A., and Hasekamp, O.: Toward Global Mapping of Methane With TROPOMI: First Results and Intersatellite Comparison to GOSAT, Geophysical Research Letters, 45, 3682–3689, https://doi.org/10.1002/2018GL077259, 2018.

Häffner, L.: Specification of Target Quantities for the Evaluation of the Capabilities of Future Observing Networks, https://avengers-project.eu/wp-content/uploads/2024/11/AVENGERS_Deliverable_D1.2.pdf, 2024.

Imasu, R., Matsunaga, T., Nakajima, M., Yoshida, Y., Shiomi, K., Morino, I., Saitoh, N., Niwa, Y., Someya, Y., Oishi, Y., Hashimoto, M., Noda, H., Hikosaka, K., Uchino, O., Maksyutov, S., Takagi, H., Ishida, H., Nakajima, T. Y., Nakajima, T., and Shi, C.: Greenhouse gases Observing SATellite 2 (GOSAT-2): mission overview, Progress in Earth and Planetary Science, 10, 33, https://doi.org/10.1186/s40645-023-00562-2, 2023.

IPCC: Climate Change 2021: The Physical Science Basis. Contribution of Working Group I to the Sixth Assessment Report of the Intergovernmental Panel on Climate Change, Cambridge University Press, Cambridge, UK and New York, NY, USA, https://doi.org/10.1017/9781009157896, 2021.

IPCC: Climate Change 2022: Mitigation of Climate Change. Contribution of Working Group III to the Sixth Assessment Report of the Intergovernmental Panel on Climate Change, Cambridge University Press, Cambridge, UK and New York, NY, USA, https://doi.org/10.1017/9781009157926, 2022.

Irakulis-Loitxate, I., Guanter, L., Liu, Y.-N., Varon, D. J., Maasakkers, J. D., Zhang, Y., Chulakadabba, A., Wofsy, S. C., Thorpe, A. K., Duren, R. M., Frankenberg, C., Lyon, D. R., Hmiel, B., Cusworth, D. H., Zhang, Y., Segl, K., Gorroño, J., Sánchez-García, E., Sulprizio, M. P., Cao, K., Zhu, H., Liang, J., Li, X., Aben, I., and Jacob, D. J.: Satellite-based survey of extreme methane emissions in the Permian basin, Science Advances, 7, eabf4507, https://doi.org/10.1126/sciadv.abf4507, 2021.

Irakulis-Loitxate, I., Guanter, L., Maasakkers, J. D., Zavala-Araiza, D., and Aben, I.: Satellites Detect Abatable Super-Emissions in One of the World's Largest Methane Hotspot Regions, Environmental Science & Technology, 56, 2143–2152, https://doi.org/10.1021/acs.est.1c04873, 2022.

ISO-2533: ISA Standard Atmosphere, Standard, International Organization for Standardization, 1975.

Jacob, D. J., Varon, D. J., Cusworth, D. H., Dennison, P. E., Frankenberg, C., Gautam, R., Guanter, L., Kelley, J., McKeever, J., Ott, L. E., Poulter, B., Qu, Z., Thorpe, A. K., Worden, J. R., and Duren, R. M.: Quantifying methane emissions from the global scale down to point sources using satellite observations of atmospheric methane, https://doi.org/10.5194/acp-22-9617-2022, 2022.

Jervis, D., McKeever, J., Durak, B. O. A., Sloan, J. J., Gains, D., Varon, D. J., Ramier, A., Strupler, M., and Tarrant, E.: The GHGSat-D imaging spectrometer, Atmospheric Measurement Techniques, 14, 2127–2140, https://doi.org/10.5194/amt-14-2127-2021, 2021.

Jervis, D., Girard, M., MacLean, J.-P. W., Marshall, D., McKeever, J., Strupler, M., Ramier, A., Tarrant, E., Young, D., Maasakkers, J. D., Aben, I., and Scarpelli, T. R.: Global energy sector methane emissions estimated by using facility-level satellite observations, Science, 390, 1151–1155, https://doi.org/10.1126/science.adv3183, 2025.

Knapp, M., Scheidweiler, L., Külheim, F., Kleinschek, R., Necki, J., Jagoda, P., and Butz, A.: Spectrometric imaging of sub-hourly methane emission dynamics from coal mine ventilation, Environmental Research Letters, 18, 044 030, https://doi.org/10.1088/1748-9326/acc346, 2023.

Kuhlmann, G., Broquet, G., Marshall, J., Clément, V., Löscher, A., Meijer, Y., and Brunner, D.: Detectability of CO_2 emission plumes of cities and power plants with the Copernicus Anthropogenic CO_2 Monitoring (CO2M) mission, Atmospheric Measurement Techniques, 12, 6695–6719, https://doi.org/10.5194/amt-12-6695-2019, 2019.

Kuze, A., Suto, H., Nakajima, M., and Hamazaki, T.: Thermal and near infrared sensor for carbon observation Fourier-transform spectrometer on the Greenhouse Gases Observing Satellite for greenhouse gases monitoring, Applied Optics, 48, 6716–6733, https://doi.org/10.1364/AO.48.006716, 2009.

LISIRD: TSIS-1 Hybrid Solar Reference Spectrum (HSRS), Full Resolution, https://lasp.colorado.edu/lisird/data/tsis1_hsrs_p1nm, 2022.

Lorente, A., Borsdorff, T., Butz, A., Hasekamp, O., aan de Brugh, J., Schneider, A., Wu, L., Hase, F., Kivi, R., Wunch, D., Pollard, D. F., Shiomi, K., Deutscher, N. M., Velazco, V. A., Roehl, C. M., Wennberg, P. O., Warneke, T., and Landgraf, J.: Methane retrieved from TROPOMI: improvement of the data product and validation of the first 2 years of measurements, Atmospheric Measurement Techniques, 14, 665–684, https://doi.org/10.5194/amt-14-665-2021, 2021.

Manolakis, D., Truslow, E., Pieper, M., Cooley, T., and Brueggeman, M.: Detection Algorithms in Hyperspectral Imaging Systems: An Overview of Practical Algorithms, IEEE Signal Processing Magazine, 31, 24–33, https://doi.org/10.1109/MSP.2013.2278915, 2014.

https://doi.org/10.5194/egusphere-2026-3730
Preprint. Discussion started: 17 July 2026

Meerdink, S. K., Hook, S. J., Roberts, D. A., and Abbott, E. A.: The ECOSTRESS spectral library version 1.0, Remote Sensing of Environment, 230, 111 196, https://doi.org/10.1016/j.rse.2019.05.015, 2019.

METI and NASA: ASTER Global Digital Elevation Model V003, https://search.earthdata.nasa.gov/search, 2019.

Nieke, J., Despoisse, L., Gabriele, A., Weber, H., Strese, H., Ghasemi, N., Gascon, F., Alonso, K., Boccia, V., Tsonevska, B., Choukroun, P., Ottavianelli, G., and Celesti, M.: The copernicus hyperspectral imaging mission for the environment (CHIME): an overview of its mission, system and planning status, p. 7, https://doi.org/10.1117/12.2679977, 2023.

Nisbet, E. G., Fisher, R. E., Lowry, D., France, J. L., Allen, G., Bakkaloglu, S., Broderick, T. J., Cain, M., Coleman, M., Fernandez, J., Forster, G., Griffiths, P. T., Iverach, C. P., Kelly, B. F. J., Manning, M. R., Nisbet-Jones, P. B. R., Pyle, J. A., Townsend-Small, A., al Shalaan, A., Warwick, N., and Zazzeri, G.: Methane Mitigation: Methods to Reduce Emissions, on the Path to the Paris Agreement, Reviews of Geophysics, 58, e2019RG000 675, https://doi.org/10.1029/2019RG000675, 2020.

Ocko, I. B., Sun, T., Shindell, D., Oppenheimer, M., Hristov, A. N., Pacala, S. W., Mauzerall, D. L., Xu, Y., and Hamburg, S. P.: Acting rapidly to deploy readily available methane mitigation measures by sector can immediately slow global warming, Environmental Research Letters, 16, 054 042, https://doi.org/10.1088/1748-9326/abf9c8, 2021.

Paris Agreement: United Nations: Paris Agreement, https://unfccc.int/process-and-meetings/the-paris-agreement/, 2016.

Parker, R. J., Boesch, H., Byckling, K., Webb, A. J., Palmer, P. I., Feng, L., Bergamaschi, P., Chevallier, F., Notholt, J., Deutscher, N., Warneke, T., Hase, F., Sussmann, R., Kawakami, S., Kivi, R., Griffith, D. W. T., and Velazco, V.: Assessing 5 years of GOSAT Proxy XCH_4 data and associated uncertainties, Atmospheric Measurement Techniques, 8, 4785–4801, https://doi.org/10.5194/amt-8-4785-2015, 2015.

Pei, Z., Han, G., Mao, H., Chen, C., Shi, T., Yang, K., Ma, X., and Gong, W.: Improving quantification of methane point source emissions from imaging spectroscopy, Remote Sensing of Environment, 295, 113 652, https://doi.org/10.1016/j.rse.2023.113652, 2023.

Reuter, M., Hilker, M., Noël, S., Di Noia, A., Weimer, M., Schneising, O., Buchwitz, M., Bovensmann, H., Burrows, J. P., Bösch, H., and Lang, R.: Retrieving the atmospheric concentrations of carbon dioxide and methane from the European Copernicus CO2M satellite mission using artificial neural networks, Atmospheric Measurement Techniques, 18, 241–264, https://doi.org/10.5194/amt-18-241-2025, 2025.

Roger, J., Irakulis-Loitxate, I., Valverde, A., Gorroño, J., Chabrillat, S., Brell, M., and Guanter, L.: High-Resolution Methane Mapping with the EnMAP Satellite Imaging Spectroscopy Mission, IEEE Transactions on Geoscience and Remote Sensing, 62, 1–12, https://doi.org/10.1109/TGRS.2024.3352403, 2024.

Saunois, M., Martinez, A., Poulter, B., Zhang, Z., Raymond, P. A., Regnier, P., Canadell, J. G., Jackson, R. B., Patra, P. K., Bousquet, P., Ciais, P., Dlugokencky, E. J., Lan, X., Allen, G. H., Bastviken, D., Beerling, D. J., Belikov, D. A., Blake, D. R., Castaldi, S., Crippa, M., Deemer, B. R., Dennison, F., Etiope, G., Gedney, N., Höglund-Isaksson, L., Holgerson, M. A., Hopcroft, P. O., Hugelius, G., Ito, A., Jain, A. K., Janardanan, R., Johnson, M. S., Kleinen, T., Krummel, P. B., Lauerwald, R., Li, T., Liu, X., McDonald, K. C., Melton, J. R., Mühle, J., Müller, J., Murguia-Flores, F., Niwa, Y., Noce, S., Pan, S., Parker, R. J., Peng, C., Ramonet, M., Riley, W. J., Rocher-Ros, G., Rosentreter, J. A., Sasakawa, M., Segers, A., Smith, S. J., Stanley, E. H., Thanwerdas, J., Tian, H., Tsuruta, A., Tubiello, F. N., Weber, T. S., van der Werf, G. R., Worthy, D. E. J., Xi, Y., Yoshida, Y., Zhang, W., Zheng, B., Zhu, Q., Zhu, Q., and Zhuang, Q.: Global Methane Budget 2000–2020, Earth System Science Data, 17, 1873–1958, https://doi.org/10.5194/essd-17-1873-2025, 2025.

Schneising, O., Buchwitz, M., Reuter, M., Bovensmann, H., Burrows, J. P., Borsdorff, T., Deutscher, N. M., Feist, D. G., Griffith, D. W. T., Hase, F., Hermans, C., Iraci, L. T., Kivi, R., Landgraf, J., Morino, I., Notholt, J., Petri, C., Pollard, D. F., Roche, S., Shiomi, K., Strong, K., Sussmann, R., Velazco, V. A., Warneke, T., and Wunch, D.: A scientific algorithm to simultaneously retrieve carbon monoxide and methane from TROPOMI onboard Sentinel-5 Precursor, Atmospheric Measurement Techniques, 12, 6771–6802, https://doi.org/10.5194/amt-12-6771-2019, 2019.

Sierk, B., Fernandez, V., Bézy, J.-L., Meijer, Y., Durand, Y., Courrèges-Lacoste, G. B., Pachot, C., Löscher, A., Nett, H., Minoglou, K., Boucher, L., Windpassinger, R., Pasquet, A., Serre, D., and Hennepe, F. t.: The Copernicus CO2M mission for monitoring anthropogenic carbon dioxide emissions from space, in: International Conference on Space Optics — ICSO 2020, vol. 11852, pp. 1563–1580, SPIE, https://doi.org/10.1117/12.2599613, 2021.

Storch, T., Honold, H.-P., Chabrillat, S., Habermeyer, M., Tucker, P., Brell, M., Ohndorf, A., Wirth, K., Betz, M., Kuchler, M., Mühle, H., Carmona, E., Baur, S., Mücke, M., Löw, S., Schulze, D., Zimmermann, S., Lenzen, C., Wiesner, S., Aida, S., Kahle, R., Willburger, P., Hartung, S., Dietrich, D., Plesia, N., Tegler, M., Schork, K., Alonso, K., Marshall, D., Gerasch, B., Schwind, P., Pato, M., Schneider, M., de los Reyes, R., Langheinrich, M., Wenzel, J., Bachmann, M., Holzwarth, S., Pinnel, N., Guanter, L., Segl, K., Scheffler, D., Foerster, S., Bohn, N., Bracher, A., Soppa, M. A., Gascon, F., Green, R., Kokaly, R., Moreno, J., Ong, C., Sornig, M., Wernitz, R., Bagschik, K., Reintsema, D., La Porta, L., Schickling, A., and Fischer, S.: The EnMAP imaging spectroscopy mission towards operations, Remote Sensing of Environment, 294, 113 632, https://doi.org/10.1016/j.rse.2023.113632, 2023.

Thompson, D. R., Leifer, I., Bovensmann, H., Eastwood, M., Fladeland, M., Frankenberg, C., Gerilowski, K., Green, R. O., Kratwurst, S., Krings, T., Luna, B., and Thorpe, A. K.: Real-time remote detection and measurement for airborne imaging spectroscopy: a case study with methane, Atmospheric Measurement Techniques, 8, 4383–4397, https://doi.org/10.5194/amt-8-4383-2015, 2015.

Thompson, D. R., Thorpe, A. K., Frankenberg, C., Green, R. O., Duren, R., Guanter, L., Hollstein, A., Middleton, E., Ong, L., and Ungar, S.: Space-based remote imaging spectroscopy of the Aliso Canyon CH4 superemitter, Geophysical Research Letters, 43, 6571–6578, https://doi.org/10.1002/2016GL069079, 2016.

Thorpe, A. K., Roberts, D. A., Bradley, E. S., Funk, C. C., Dennison, P. E., and Leifer, I.: High resolution mapping of methane emissions from marine and terrestrial sources using a Cluster-Tuned Matched Filter technique and imaging spectrometry, Remote Sensing of Environment, 134, 305–318, https://doi.org/10.1016/j.rse.2013.03.018, 2013.

Thorpe, A. K., Frankenberg, C., and Roberts, D. A.: Retrieval techniques for airborne imaging of methane concentrations using high spatial and moderate spectral resolution: application to AVIRIS, Atmospheric Measurement Techniques, 7, 491–506, https://doi.org/10.5194/amt-7-491-2014, 2014.

Thorpe, A. K., Frankenberg, C., Aubrey, A. D., Roberts, D. A., Nottrott, A. A., Rahn, T. A., Sauer, J. A., Dubey, M. K., Costigan, K. R., Arata, C., Steffke, A. M., Hills, S., Haselwimmer, C., Charlesworth, D., Funk, C. C., Green, R. O., Lundeen, S. R., Boardman, J. W., Eastwood, M. L., Sarture, C. M., Nolte, S. H., Mccubbin, I. B., Thompson, D. R., and McFadden, J. P.: Mapping methane concentrations from a controlled release experiment using the next generation airborne visible/infrared imaging spectrometer (AVIRIS-NG), Remote Sensing of Environment, 179, 104–115, https://doi.org/10.1016/j.rse.2016.03.032, 2016.

Thorpe, A. K., Green, R. O., Thompson, D. R., Brodrick, P. G., Chapman, J. W., Elder, C. D., Irakulis-Loitxate, I., Cusworth, D. H., Ayasse, A. K., Duren, R. M., Frankenberg, C., Guanter, L., Worden, J. R., Dennison, P. E., Roberts, D. A., Chadwick, K. D., Eastwood, M. L., Fahlen, J. E., and Miller, C. E.: Attribution of individual methane and carbon dioxide emission sources using EMIT observations from space, Science Advances, 9, eadh2391, https://doi.org/10.1126/sciadv.adh2391, 2023.

Valverde, A., Irakulis-Loitxate, I., Gorroño, J., Pei, Z., and Guanter, L.: Satellite-based assessment of methane emissions from the Darvaza gas crater, https://eartharxiv.org/repository/view/9468/, 2025.

https://doi.org/10.5194/egusphere-2026-3730
Preprint. Discussion started: 17 July 2026

Varon, D. J., Jacob, D. J., McKeever, J., Jervis, D., Durak, B. O. A., Xia, Y., and Huang, Y.: Quantifying methane point sources from fine-scale satellite observations of atmospheric methane plumes, Atmospheric Measurement Techniques, 11, 5673–5686, https://doi.org/10.5194/amt-11-5673-2018, 2018.

Veefkind, J. P., Aben, I., McMullan, K., Förster, H., de Vries, J., Otter, G., Claas, J., Eskes, H. J., de Haan, J. F., Kleipool, Q., van Weele, M., Hasekamp, O., Hoogeveen, R., Landgraf, J., Snel, R., Tol, P., Ingmann, P., Voors, R., Kruizinga, B., Vink, R., Visser, H., and Levelt, P. F.: TROPOMI on the ESA Sentinel-5 Precursor: A GMES mission for global observations of the atmospheric composition for climate, air quality and ozone layer applications, Remote Sensing of Environment, 120, 70–83, https://doi.org/10.1016/j.rse.2011.09.027, 2012.

Yoshida, Y., Ota, Y., Eguchi, N., Kikuchi, N., Nobuta, K., Tran, H., Morino, I., and Yokota, T.: Retrieval algorithm for CO_2 and CH_4 column abundances from short-wavelength infrared spectral observations by the Greenhouse gases observing satellite, Atmospheric Measurement Techniques, 4, 717–734, https://doi.org/10.5194/amt-4-717-2011, 2011.